RESONANCE RAMAN SCATTERING AND OPTICAL REFLECTIVITY STUDIES OF ION IMPLANTATION-PRODUCED DAMAGE IN CUPROUS OXIDE

BY

JOSEPH FREDRICK HESSE

B.S., University of Nebraska, 1974

A MASTER'S THESIS

submitted in partial fulfillment of the

requirements for the degree

MASTER OF SCIENCE

Department of Physics

KANSAS STATE UNIVERSITY
Manhattan, Kansas

1977

Approved by:

Major Professor

ACKNOWLEDGEMENTS

This Thesis is dedicated to Amber whose patience, encouragement, understanding, and typing throughout the course of its development made it possible. Special thanks is given to my major professor, Alvin Compaan, whose guidance in and outside the laboratory helped me to understand physics a little better.

The work and cooperation of S. C. Abbi in the early stages of sample annealing, and the valuable assistance of Dr. J. R. MacDonald for the ion implantation on his low energy accelerator are both gratefully appreciated. We are grateful to R. A. Forman of the National Bureau of Standards, Washington, D. C. for providing the samples of Cu_2O, to Dr. R. D. Dragsdorf and Dr. R. S. Lee for serving on my committee. Many helpful discussions with Robert M. Habiger are gratefully appreciated.

Contents

Figure page

Table

I. INTRODUCTION

A. General

Ion implantation has become a highly successful method to dope semiconductors and insulators with various types of ions in order to enhance electrical, optical, and photovoltaic properties so as to make these types of materials more efficient and suitable for applications in technology, such as solar cells. Beams of energetic, charged particles are incident onto and eventually come to rest at some depth within a crystal after they lose their kinetic energy through atomic and nuclear collisions with the atoms of the crystal lattice. Atomic scattering processes generally result in electronic excitations whereas nuclear scattering processes result in the displacement of the lattice atoms. Thus if the nuclear collisions are the dominant energy loss mechanism, large numbers of lattice atoms (up to 10^3/incident ion) are generally displaced from their initial sites and may become randomly scattered in a small region about the path of the initial ion through the crystal. This random scattering of the lattice atoms constitutes damage in the crystal. Generally such damage greatly affects the properties of the crystal such as its electrical conductivity and optical absorption. However, annealing is often successful in removing much of this damage, although care is required to choose anneal temperatures low enough to prevent significant diffusion of the implanted ions.

In this thesis, we report on a study of ion implantation produced damage in cuprous oxide (Cu_2O). A convenient monitor of such damage and its annealing is phonon Raman scattering. Phonons result from the motion of the lattice atoms. Loss of the periodicity of the lattice is expected

to change the intensities of the Raman features. Resonant Raman scattering should show more pronounced changes in the Raman intensities because of strong coupling to exciton states which are also affected by damage. Recently, several Raman scattering damage studies have been done on Cu_2O in this laboratory. Broadening of exciton states has been attributed to surface damage induced by mechanical polishing.[1] An ion implantation dose dependence study using phonon Raman scattering with laser frequencies nearly resonant with intrinsic exciton states in Cu_2O revealed damaged saturation at a dose of 10^{15} Cd ions/cm^2. In this thesis we have extended these phonon Raman studies of implantation-produced damage to monitoring progressive anneal stages of Cu_2O for series of isochronal (constant time periods) and isothermal (constant temperature) anneal treatments. Rapid increases in Raman intensities of two orders of magnitude occur with anneal treatments to approximately 300°C with strong annealing occuring at ~250°C demonstrating the sensitivity of resonance Raman scattering to damage annealing. We also made some optical reflectivity studies which revealed the broadening of exciton states in the damaged samples and the narrowing of these states during the series of anneal treatments. These reflectivity studies help to interpret our present work and to verify the interpretations of previous work[1, 2] on Cu_2O.

In this introduction, I shall survey other methods used to probe lattice damage due to ion implantation in such semiconductors as GaAs and GaP with an emphasis on their sensitivty to damage. Though by no means an exhaustive survey, it serves as an introduction to damage monitoring probes. Following this review of probes, we discuss damage

production in crystals during ion implantation, Raman scattering, optical reflectivity, and annealing processes. In the rest of this thesis we present our optical experiments with which we probe the annealing behavior of ion implanted Cu_2O.

B. Methods of Damage Detection

A variety of methods have been used to study lattice damage in crystals. In many cases the experimental system one has at hand and, of more importance, the type of information one desires determines the particular method that is used. Methods of damage detection of interest here are:

a) Cathodoluminescence

b) Ellipsometry

c) Channeling and Back scattering

d) Electrical Measurements

e) Infrared Studies

f) Optical Studies

Cathodoluminescence

Energetic electrons incident upon a crystal lose their energy to the crystal atoms through atomic excitations with the production of electron-hole pairs. The electron-hole pairs then recombine radiatively causing the crystal to luminesce. The intensity of this luminescence increases as the energy of the electrons (of the beam voltage) increases because larger numbers of electron-hole pairs are created. In cathodoluminescence, the intensity of this luminescence is measured as a function of

electron beam voltage and with the aid of electron stopping curves the depth of the luminescing centers may be resolved. For ion implanted materials, changes in the luminescence spectra from those of pure samples yields information on locations of luminescence centers due to the presence of the implanted ions.

Though several studies[3, 4] of cathodoluminescence have been done on implanted semiconductors, no damage dependence studies were reported. The relative concentration of luminescing centers as a function of depth was the central focus of the studies. Problems arise in attempts to utilize cathodoluminescence for annealing studies because of reported changes[4] occurring in the luminescence spectrum during the electron irradiation so that it may be an unreliable probe for such studies although it may be useful for determing the depths of implanted ions.

Ellipsometry

In ellipsometry, analysis of the polarization of reflected monochromatic light as a function of the angle of incidence determines optical constants such as the index of refraction. A lattice damage study[5] using this technique reports that changes in the optical constants were observed for various anneal stages in Ar^+ implanted GaAs but the results were inconclusive because they are easily dependent on surface purity and were thus difficult to reproduce. So it is not very dependable as a probe. Also it may become very lengthy since one is more interested in the spectral dependence of the optical constants and such a scan over a variety of frequencies could be time consuming.

Ellipsometric measurements are also done using white light but then changes in optical constants with annealing would tend to be small since a change at one frequency may be washed out by an opposite change at another frequency of light.

Channeling and Back scattering Studies

With channeling studies[5, 6] a mono-energetic beam of light ions such as He^+ is incident on a previously implanted crystal along one of the crystal axis. The He^+ scattered by the lattice atoms and by the previously implanted ions are detected in a back scattered configuration. For a pure, well ordered lattice, few light ions are back scattered when initially aligned along a crystal axis while an implanted sample will contain many atoms which occupy sites in the space of a channel direction so that the light ions will scatter off these atoms. A detector at ~160° from the incident direction detects the back scattered ions and the resulting energy spectrum, with the aid of the stopping power for the probing ions, is analyzed to determine the positions of the displaced atoms and implanted ions in the crystal. In this respect, this method is similar to cathodoluminescence discussed earlier.

A dose dependence study[4] produced increases of less than 20% in the back scattered yield as the dose increased from 10^{11} to 10^{15} ions/cm^2 for Ar^+ into GaAs. However, a temperature dependence was observed showing that the back scattered yield for implantation at 100 K was nearly an order of magnitude larger than the yield on a room temperature implant of oxygen into GaP.[6] Therefore back scattering is not a very sensitive probe

to study damage annealing except perhaps for low temperature implantations where self annealing is kept low. However, backscattering does give information on the lattice positions of the implanted ions. Also back scattering is a destructive probe since the probing ions themselves produce damage in the crystal. We note here that cathodoluminescence is not as destructive a probe as back scattering since the cathodoluminescence probing beam is composed of electrons which are much lighter than the ions (usually He^+) typically used in back scattering experiments, and therefore, the electron would not be able to transfer much momentum to the crystal lattice for purposes of damage production.

Electrical Measurements

Sheet conductivity measurements have been used[7] to study the isothermal annealing of defects in phosphorous bombarded silicon. The derivative of the sheet conductivity is found to decrease by a factor of ~10 during an anneal time of 35 minutes at 36°C.

A dose dependence and annealing study of damage in GaAs implanted with various ions was done recently.[8] Data revealed the sheet resistivity to decrease by up to a factor of 100 as the ion doses increased by a factor of 10. It was also found that the sheet resistivity increased by $\sim 10^3$ with annealing from 0 to 500°C.

Infrared Studies

Infrared reflectivity and infrared absorption are two experimental techniques often used for damage-annealing studies.[9, 10, 11] For infrared reflectivity, infrared (I.R.) radiation is reflected off a polished surface at near normal incidence and analysis of the reflected light

shows the selective reflection of the radiation by the crystal as a function of energy E. The spectrum is usually plotted showing the percent of radiation reflected at an energy E_i:

$$R(\%) = I_R(E_i)/I_o(E_i) \times 100$$

where $I_o(E_i)$ is the incident intensity at E_i and $I_R(E_i)$ is the reflected intensity at E_i. The features in the reflectivity spectrum are characteristic of the infrared active phonons of the crystal.

Infrared reflectivity has been used to study the damage in N^+ implanted GaAs[9] and GaP.[11] Dose dependence studies showed decreases in reflectivity peaks from R~100% to R~40% while nearly complete recovery of the pre-implantation reflectivity occurs with annealing to 300°C.

Infrared absorption is complementary to reflectivity. While probably not any more sensitive to damage annealing, absorption is useful in those cases where the reflectivity of a crystal is small. Its chief disadvantage probably lines in the fact that with implantation damaged crystals, the implantation depth $t << D$, the crystal thickness, so that most of the transmitted light is from the undamaged portion of the crystal and hence effects due to damage would tend to be masked by the undamaged region.

Optical Absorption

Transmitted visible light is analyzed to yield the selective absorption of it by the crystal. Studies in GaP[12] reveal a shift of the optical absorption edge frequency from 2.2 eV to 1 eV as damage increases due to Ar^+ from doses up to 10^{15} ions/cm^2. This is a large shift since

1 ev = 8065 cm^{-1} and shifts as small as 1 cm^{-1} are detectable in the visible region. The original absorption edge was recovered after annealing to 500°C. This is expected since perturbations in the lattice broaden the band edges and thus decrease the gap energy difference. Optical absorption is limited though to thin films for cases of strongly absorbing materials like GaAs and it then becomes necessary to use other techniques like optical reflectivity.

Optical Reflectivity

Like its counterpart in the infrared region of the spectrum, optical reflectivity displays the selective reflection of visible light by a sample surface for near normal incidence. The features in this spectrum represent the electronic states of the crystal and also the reflectivity spectrum can be analyzed to determine the optical constants in the visible region. For optically opaque materials, reflectivity measurements are more suitable than absorption measurements and if one is studying surface damage effects, then depending on the absorption of the crystal at some frequency and on the implanted ion depth, one can probe only the implanted layers most of the time.

Dose dependence studies and annealing studies have been reported [5, 6, 13] on GaAs implanted with heavy ions such as Cd^+ to doses of 10^{15} ions/cm^2. Large changes in the reflectance occurs with the overall trend towards constant reflectance as the ion dose increases, ie. the various features flatten out, but the pre-implantation reflectivity is recovered with anneal temperatures of 200 - 300°C.[13]

Raman Scattering

Phonon Raman scattering has been used to study ion implantation-produced damage. Broadening of phonon modes as a function of ion dose is observed in Xe^+ implanted GaAs.[11] 488.0 and 514.5 nm laser excitation is used to monitor the annealing of N^+ implanted GaP to temperatures of 500°C. Increases in Raman peak heights of nearly two orders of magnitude occur as annealing progresses along with narrowing of the phonon modes.[11]

II. Techniques

A. Ion Implantation[15]

Ion implantation provides a very useful and flexible method by which we can introduce impurities into semiconductors. Diffusion methods of doping are equilibrium processes which depend upon the temperature and the impurity concentration gradient. But not all impurity materials can diffuse into any host crystal so that ion implantation provides a convenient alternative to diffusion. The ability to select the type of ion and its incident energy allows one to control the dopant profile (density of ions as a function of depth) while control of the ion dose determines the density of ions in the sample and the amount of damage produced. By orienting one of the crystal axis parallel to the direction of the ion beam we can substantially increase the penetration depth of the ions (called the range). This is called channeling and is not dissimilar to the channeling method for locating implanted ions using light ions. The damage which results from the ion - atom collisions, however, is highly undesirable and so may require high annealing temperatures for its removal.

Production of Damage

Depending upon the collision parameters, an energetic ion colliding with an atom of the crystal lattice transfers some of its kinetic energy and momentum to that atom. If the amount of energy transfered is less than a lower limit, E_d (called the displacement energy), the atom will remain and probably oscillate within the potential well of its lattice site. It is similar to the damped harmonic oscillator and the energy is dissipated as vibrational energy to the neighboring atoms. Energy is also expended in atomic excitations. Little or no lattice damage results. However, if the energy transfered is greater than E_d, the lattice atom is knocked out of its site is often called the primary "knock on." The primary "knock on" may itself be energetic enough to displace other atoms with the overall result being a cascade of displaced atoms. The general appearance is thought to be an ion track surrounded by a region composed of vacancies and interstitials. For 180 keV Cd^{++} implanted into Cu_2O, this region is estimated[2] to have a diameter of 15 Å and a depth or length of 375 Å. For low doses, these damage regions are rather isolated from one another. As the dose increases, the regions become more numerous and then begin to overlap. For high doses, the regions may overlap enough that the damage saturates in which case essentially no periodic lattice structure remains and heavier doses produce little additional change.

Due to the complexity of the system on the microscopic scale, many different types of lattice defects result: vacancy - interstitial pairs (Frenkel defects), in which case an atom is removed from its lattice site and locates at an interstitial site, leaving behind a vacancy; vacancy -

impurity pairs which usually form when an impurity and a vacancy migrate into the vicinity of each other; divacancies which are just two single vacancies occupying adjacent lattice sites. These types of defects and various combinations of them constitute the damage within the damage regions.

Energy Losses and Range

Having stated that not all the ion kinetic energy goes into the production of damage, we must consider two basic energy loss mechanisms: electronic stopping power (S_e) and nuclear stopping power (S_n). Electronic stopping power is the energy loss due to the interaction between the electron clouds of the ion and lattice atoms where atomic excitations usually result. Little damage occurs in this case since little momentum is transferred per lattice atom. Nuclear energy losses, on the other hand, result from large amounts of momentum transferred during collisions between the nuclei of the ions and the lattice atoms and thus become important in damage production. In this case, the lattice atom may receive enough energy from the ion to be knocked out of its initial lattice site.

Using the computer program of J.F. Gibbons and W. S. Johnson,[16] R. D. Dragsdorf, of this department, has computed values of $S_n(E)$ and $S_e(E)$ for several different ions implanted into Cu_2O. Among these ions is Cd^{++} ranging in energy from 10 to 200 keV. Fig. 1 shows a plot of $S_n(E)$ and $S_e(E)$ as a function of the ion energy for several ions. From these curves it is apparent that two parameters are important, the Z of the

Fig. 1

The nuclear stopping power ($S_n(E)$) and the electronic stopping power ($S_e(E)$) as a function of ion energy for several ion species implanted into Cu_2O. The curves for Cd, Zn, and N are computed from the computer program of Johnson and Gibbons (16) by R. D. Dragsdorf. The curves for He are based upon atomic density corrections of the computed values for He into ZnS as recommended by Johnson and Gibbons.

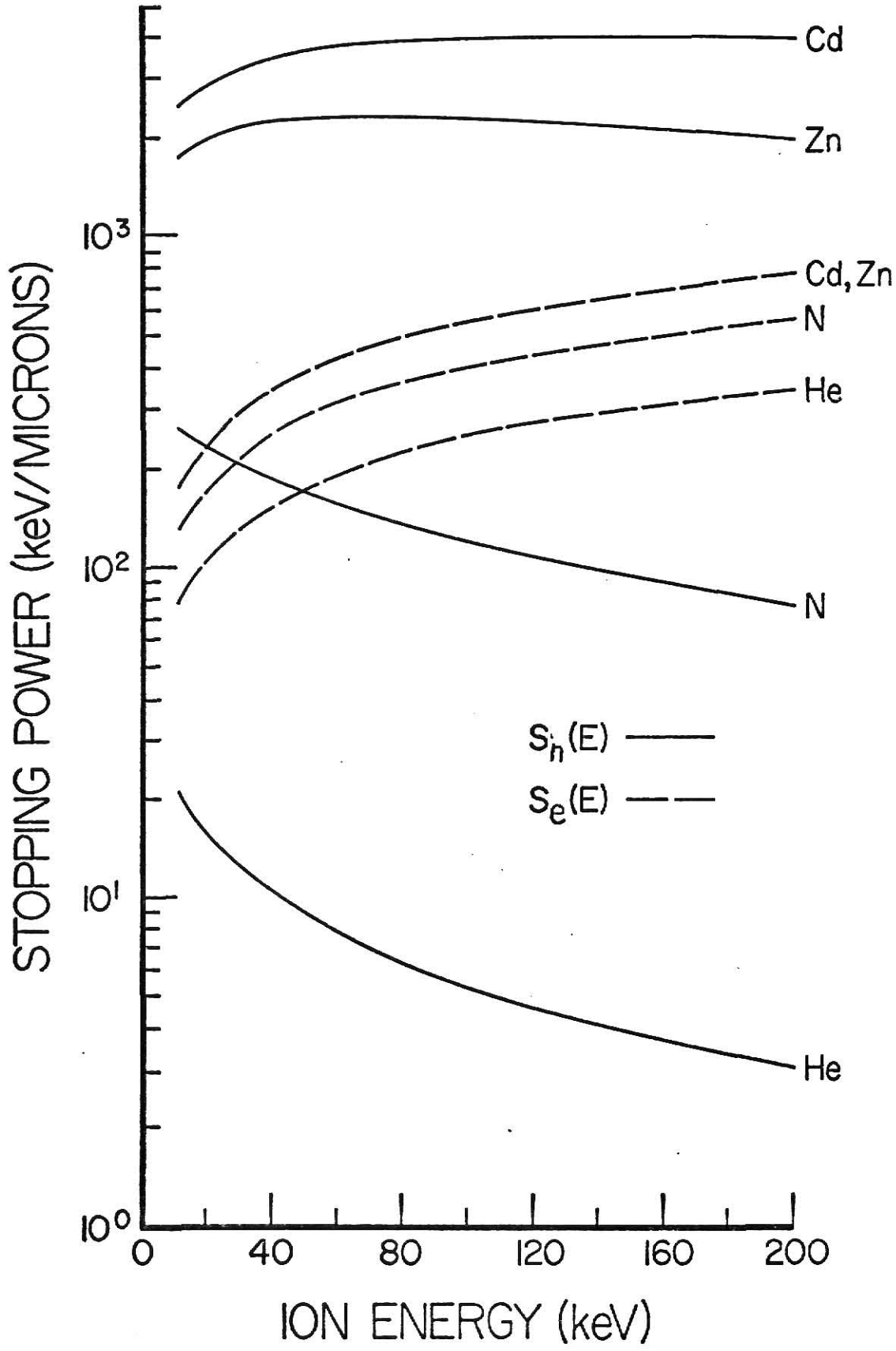
Cd
Zn
Cd, Zn
N
He
N
He
$S_n(E)$
$S_e(E)$
STOPPING POWER (keV/MICRONS)
10^3
10^2
10^1
10^0
0
40
80
120
160
200
ION ENERGY (keV)

incident ion and its energy. For heavy ions such as Cd, S_n is the dominant energy loss mechanism for energies < 200:keV. Damage is probably distributed rather uniformly throughout the lattice down to the maximum penetration of the incident ion since S_n is nearly constant in this case. For light ions (Z<20) the damage distribution picture may be different since at ion energies ~200 keV, S_e is the dominant energy loss mechanism whereas for lower ion energies, S_n gradually increases and may become larger than S_e. We expect the damage to be light near the surface of the crystal, then gradually increase in severity until it reaches a maximum near the maximum depth of the ions. Fig. 2 illustrates schematically the damage according to the LSS model for ions of energy <200 keV into Cu_2O.

The placement of ions in a lattice is a statistical process because of the large number of incident ions (>10^{12} ions/cm^2) and lattice sites involved. The ion track is different for each ion as is its depth into the crystal. This depth is just the path length along the track from the crystal surface to the ion. The important quantity is, however, the projection of this path onto the incident direction of the ion. Because this projection is generally different for each ion, we average over all implanted ions of any one type to get the projected range (R_p) of the ions. But since not all the ions are located at a depth of R_p it is also necessary to look at the distribution of ions as shown in Fig. 3a. The projected range straggling, ΔR_p, gives the average fluctuation of R_p.

For a non channeled beam of ions, we might have a distribution of ions which has a maximum density or peak at R_p and which probably shows

Fig. 2

Quantative picture of damage and ion density distribution with depth into a crystal lattice for light and heavy ions.

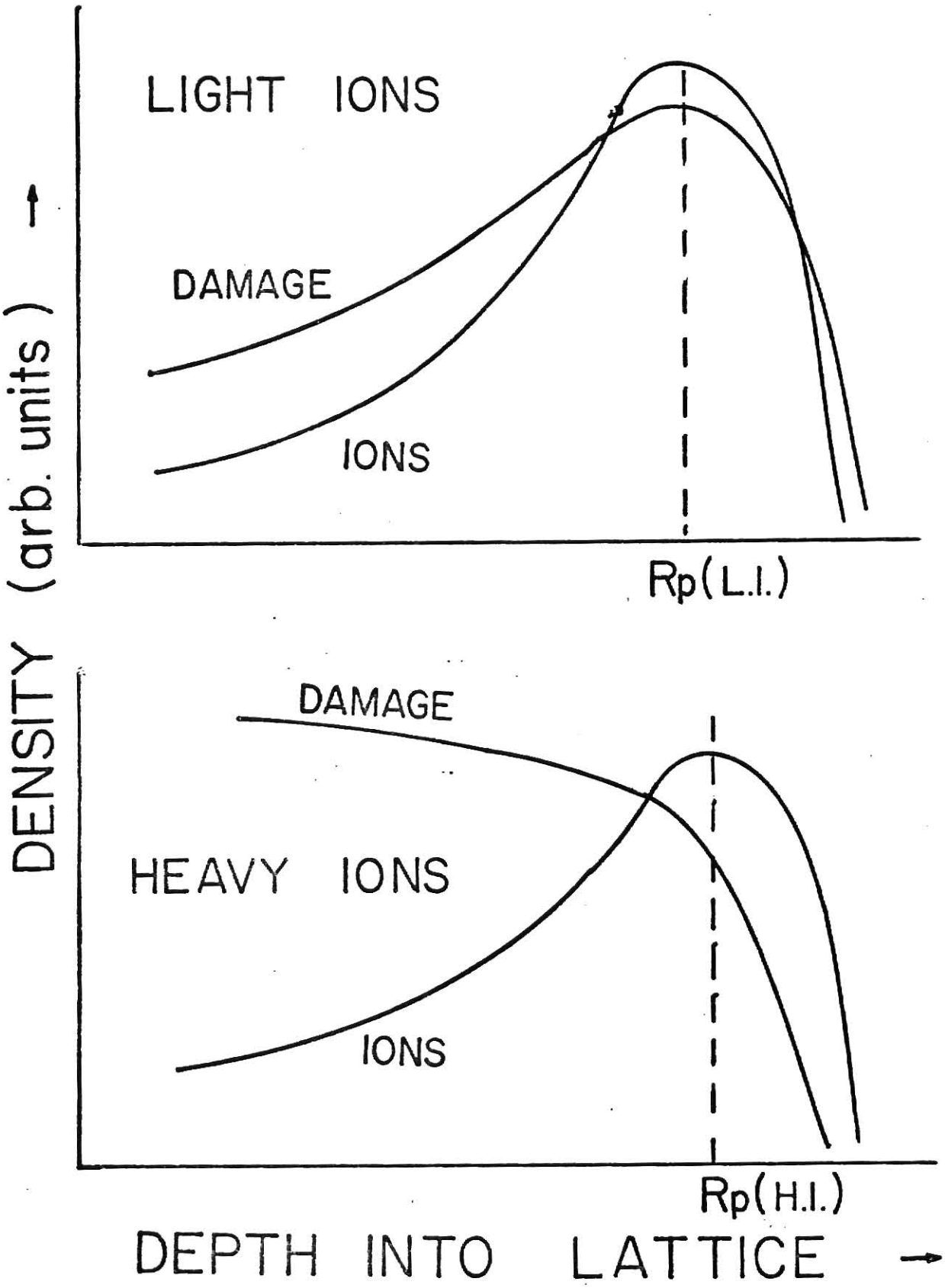
LIGHT IONS
DAMAGE
IONS
Rp(L.I.)
DENSITY (arb. units)
DAMAGE
HEAVY IONS
IONS
Rp(H.I.)
DEPTH INTO LATTICE

the behavior with ion energy as is shown in Fig. 3a. As mentioned earlier, a channeled ion will penetrate much further into the sample than an unchanneled ion so that the channeled R_p is much greater than the unchanneled R_p. For example, 40 keV P^+ into silicon have an R_p of 500 Å in an off axis direction where as $R_p \simeq 9000$ Å for the ions channeled along the [110] direction.

Calculations and estimations of projected ranges for several ions into Cu_2O have been made. From the computations by R. D. Dragsdorf for 184 keV Cd^{++} into Cu_2O, $R_p \sim .037$ microns. For He^+ and Na^+ implanted, no exact calculations are available and so several estimates were made. First of all, a compound semiconductor with nearly the same average $\bar{Z}$ (nuclear charge) per atom as Cu_2O ($\bar{Z}=22$), was selected from the table of data in Johnson and Gibbons. One such compound semiconductor is ZnS with an $\bar{Z}=23$. The data of Johnson and Gibbons lists 60 keV He^+ into ZnS as having a range of .401 microns, however no computations were made for Na^+ into ZnS. This latter problem necessitates the interpolation of the available data for ZnS.

ion	R_p
$^{10}_{Ne}$	0.1238 m
$^{11}_{Na}$	X
$^{13}_{Al}$	0.0936 m

According to Johnson and Gibbons, R_p in linear in Z for low values of Z. Then $\Delta Z_1/\Delta R_p^* = \Delta Z_2/\Delta R_p^* 2$ where $\Delta Z_1=3, \Delta Z_2=1$,

$\Delta R_{p1}^* = .0936 - .1238 \mu m = .0302$ μm so that we find

$\Delta R_{p2}^* = \bar{}(1/3)(.0302) = \bar{}.0101$ so that

$R_p(11_{Na} \rightarrow ZnS) \sim .1238 + (\bar{}.0101)\mu m = .1137 \mu m$

Fig. 3

Estimates of the ion density for arbitrary energies.

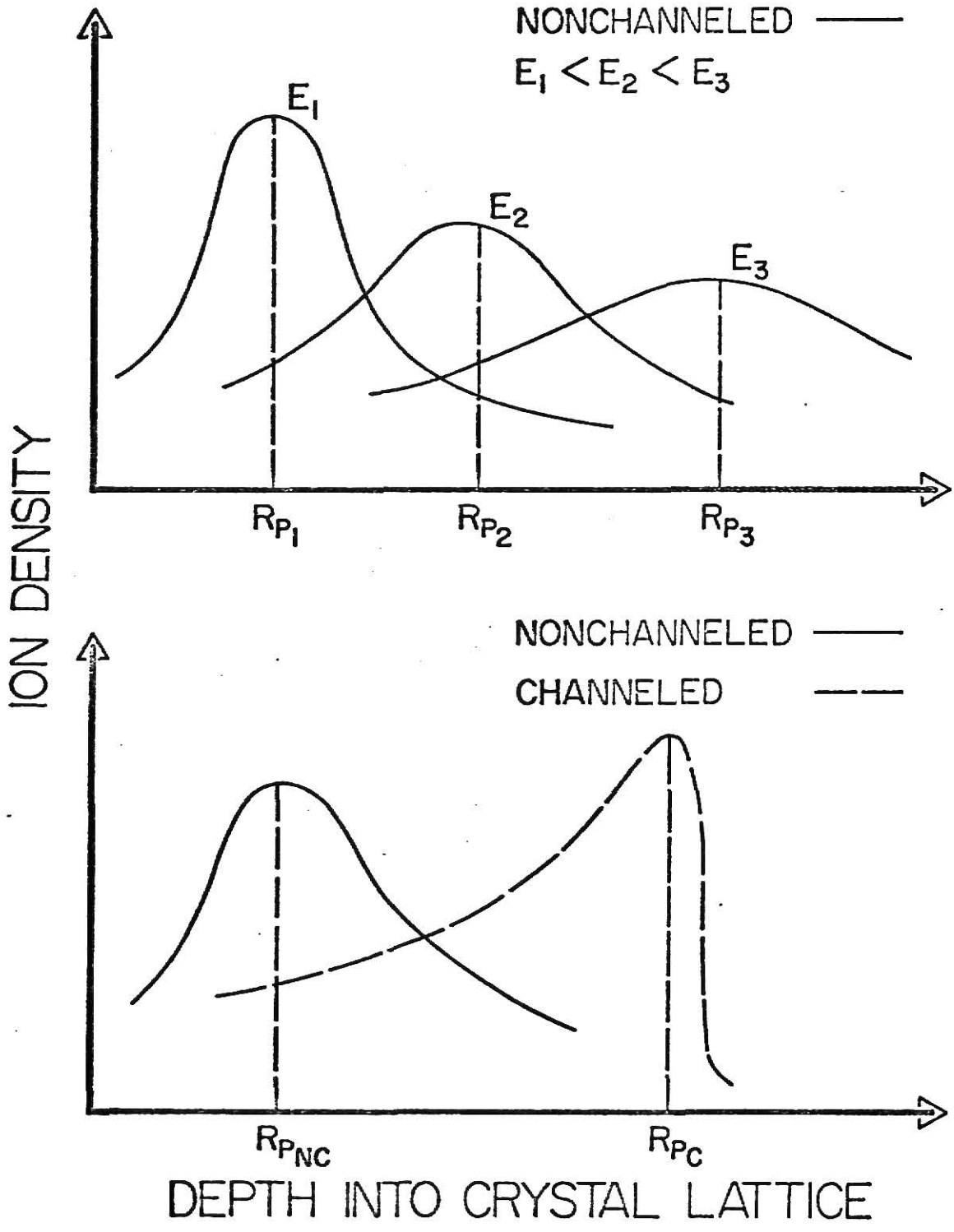
NONCHANNELED
$E_1 < E_2 < E_3$
E_1
E_2
E_3
R_{P_1}
R_{P_2}
R_{P_3}
NONCHANNELED
CHANNELED
$R_{P_{NC}}$
R_{P_C}
ION DENSITY
DEPTH INTO CRYSTAL LATTICE

However, a density correction is necessary here in order to find R_p for Cu_2O since the mass density of Cu_2O is 6.1 grams/cm^3 whereas the mass density for ZnS is 4.0 grams/cm^3. According to Johnson and Gibbons, R_p is linear in atomic mass density for compounds whose constitients are not too widely scattered about the periodic table so that all we require is a multiplicative factor to correct R_p:

$$R_p(Cu_2O)=R_p(ZnS)\times\frac{\rho(ZnS)}{\rho(Cu_2O)}$$

where ρ is the mass density of the semiconductor considered:

$$\rho(ZnS)=4.0\ gm/cm;\ \rho(Cu_2O)=6.1\ gm/cm$$

Using the above expression, we can compute R_p for several ions incident onto Cu_2O. With a similar analysis, we also find the range straggling, ΔR_p. We obtain:

ion	R_p(m)	ΔR_p(m)
60 keV He	0.263	0.079
90 keV Na	0.0745	0.029
184 keV Cd	0.037	0.010

Considerations of the projected range in ion implantation are important in many practical applications. For example, for solar cells and other light sensitive devices, incident radiation will penetrate to some depth in the material called the absorption depth. The absorption depth depends upon the physics of the material involved and upon the frequency of the radiation. In attempting to enhance the useful optical properties of a semiconductor, it becomes important for the ions to be implanted no deeper than the absorption depth of the incident light.

B. Raman Scattering

The phonon Raman effect in crystals is readily explained by using the concept of the periodicity of the crystal lattice. The transformation from the crystal lattice space to reciprocal space formulates the Brillouin Zone. Characteristic lattice vibrations, called phonons, result from considering the motion of chains of atoms in a crystal and are plotted as phonon dispersion curves since these curves illustrate the phonon frequency, Ω, as a function of position in k space (wave vector) in the Brillouin Zone out to the zone boundary. For a linear monatomic chain of atoms, only one branch exists in the phonon dispersion curve. For a crystal such as Cu_2O, which has six atoms per primitive cell, the phonon dispersion curve is rather complicated is shown in Fig. 4.

Phonon Raman Scattering

A photon of frequency w_i incident upon a crystal is absorbed by a virtual state and a scattered photon of frequency w_s is emitted along with the creation or annihilation of a phonon of frequency Ω. Such scattering is called phonon Raman scattering. While typically termed inelastic scattering because the scattered photon is shifted in energy relative to the incident photon, energy and momentum are conserved when the phonon is taken into account and we may write:

$$\hbar \vec{k_i} = h \vec{k_s} \pm h\vec{q} \qquad 1$$

$$h w_i = h w_s \pm h\Omega \qquad 2$$

for the conservation of momentum and energy respectively. $\bar{k}_i$, $\bar{k}_s$, and $\bar{q}$ are the wave vectors for the incident photon, the scattered photon

Fig. 4

Phonon dispersion curves for Cu_2O. The lower curves consisting of the dots are from inelastic thermal neutron scattering experiments (17). The solid lines here are for visibility only. The upper curves (no dots) are theoretical curves (38) based upon a simple model and are therefore not completely reliable.

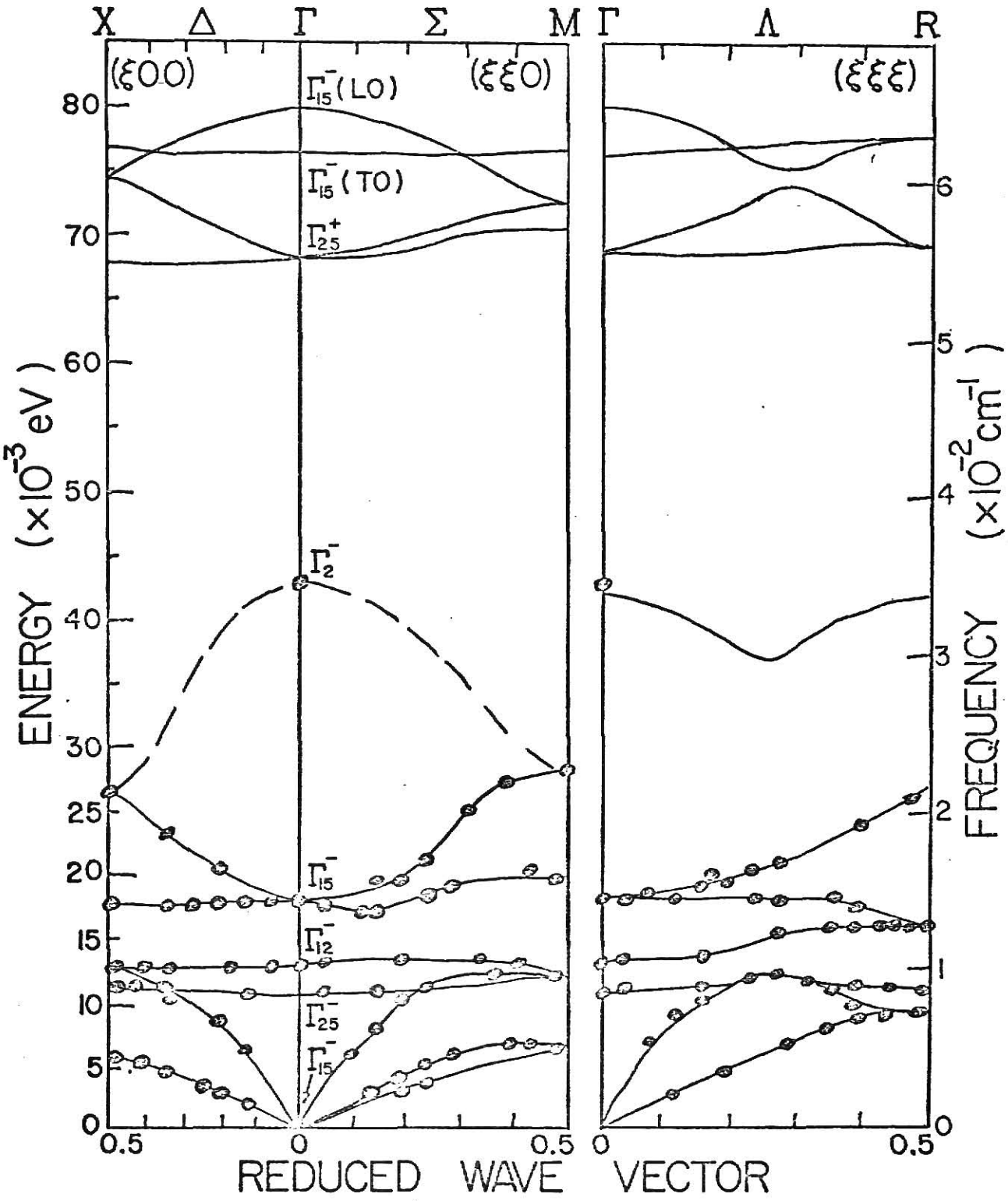
X
Δ
Γ
Σ
M
Γ
Λ
R
(ξ00)
(ξξ0)
(ξξξ)
Γ15⁻(LO)
Γ15⁻(TO)
Γ25⁺
Γ2⁻
Γ15⁻
Γ12⁻
Γ25⁻
Γ15⁻
ENERGY (×10⁻³ eV)
FREQUENCY (×10⁻² cm⁻¹)
REDUCED WAVE VECTOR
0.5
0
0.5
0
0.5

and the phonon while w_i, w_s and Ω are their respective frequencies. The - and + signs represent Anti Stokes Raman and Stokes Raman scattering.

Equation 1 tells us that the change in the photon wave vector is equal to the phonon wave vector, but from the phonon dispersion curve of Fig. 4, the frequency of the phonon depends upon location in the Brillouin Zone. If we consider the magnitude of the phonon wave vector $|\bar{q}|$ in the [100] direction of the crystal, then:

$$0 \leq |\bar{q}| \leq q_{max}$$

where $q_{max} = \pi/a$ at the zone boundary. a is the lattice constant which, for Cu_2O, equals 4.27 Å. Therefore $q_{max} = 735 \times 10^5$ cm^{-1}. The photon wave vector $k = \frac{2\pi n}{\lambda} = 3.4 \times 10^5$ cm^{-1}, where $\lambda = 480$ nm and n, the index of refraction for Cu_2O, is 2.6. We see that k is much smaller than q_{max} so that essentially zone center optic phonon participate in phonon Raman scattering.

Raman Scattering: Quantum Picture

According to second order perturbation theory, it may be shown that the Raman intensity for a scattering event is

$$I \alpha \begin{cases} |P|^2 \cdot n : \text{antistokes} \\ |P|^2 (n+1) : \text{stokes} \end{cases} \qquad 3$$

where P is a scattering matrix element, and n is the phonon population factor. P is found through third order perturbation theory and is

$$P \alpha \frac{\langle f|H_I|e_2\rangle\langle e_2|H_{II}|e_1\rangle\langle e_1|H_I|i\rangle}{(w_{e1}-w_i + i\Gamma_{e_1})(w_{e2}-w_s + i\Gamma_{e_2})} \qquad 4$$

$|i\rangle$ and $|f\rangle$ are the initial and final states of the crystal, $|e_1\rangle$ and $|e_2\rangle$ are intermediate electronic states, H_I is the Hamiltonian responsible for scattering the initial and the final states into intermediate electronic states with absorption and emission of photons, and H_{II} is the Hamiltonian responsible for scattering the state $|e_1\rangle$ into $|e_2\rangle$ with the simultaneous absorption or emission of a phonon. w_i and w_s are the incident and scattered photon frequencies, w_{e1} and w_{e2} represent the frequencies of the intermediate electronic states. These electronic states may be real or virtual, though in this thesis they are real intrinsic exciton states. $\Gamma = \frac{1}{\tau}$ where τ is the lifetime of the electronic state and Γ represents its natural width.

The expression for P contains resonance behavior when the energy of the scattered photon is equal to that of the electronic state $|e_2\rangle$, then Γ_{e_2} becomes the dominant term in the denominator of P.

The phonon population factor, n, is

$$n = \frac{1}{e^{\frac{h\Omega}{kT}} - 1} \qquad 5$$

Using this we may find the temperature dependence of the phonon Raman scattered intensities. At low temperatures (T<200K)

$$n \simeq e^{-\frac{h\Omega}{kt}}$$

and

$$I_s \propto n+1 \cong e^{-\frac{h\Omega}{kT}} + 1 \qquad 6$$

for first order Stokes scattering. We see that as T increases, I increases (assuming P does not depend too strongly on temperature). For higher order scattering,

$$I_s^{\gamma} \alpha \left(e^{\frac{-h\Omega}{kT}} + 1\right)^{\gamma} \qquad 7$$

where γ is the order of the scattering.

We recall that phonon Raman scattering was limited to the center of the Brillouin Zone for a pure, undamaged crystal. With the loss of the periodicity of the lattice, the analysis which led to the concept of the Brillouin Zone is no longer valid. Conservation of mementum then need not apply and we may have scattering from any part of the phonon dispersion curve. From Fig. 4, we see that $\frac{dw}{dq}$ is small for optic phonons at the center of the Brillouin zone. The density of phonon modes, D(w), becomes large here since $D(w) \alpha \frac{1}{dw/dq}$. This tells us that the number of optic phonons available for scattering is large at the zone center and we may therefore observe a Raman scattered photon. However, $\frac{dw}{dq}$ is also small at the zone boundary so that D(w) is large here too. Therefore, with the relaxation of the scattering selection rules, phonons at the boundary may also scatter photons. Thus additional Raman peaks may arise due to this scattering at the Brillouin zone boundary.

C. Optical Reflectivity

The optical reflectivity of Cu_2O is of interest here because of its importance in the interpretation of the resonance Raman spectra for the damaged crystal lattice. The optical reflectivity of the sample was

measured from 19,000 cm^{-1} to 23,000 cm^{-1}. In this range of frequency two prominent features occur at 20,850 cm^{-1} and 21,900 cm^{-1} which are attributed to hydrogenic exciton states just below the Γ_8^- conduction band and which result from electronic transitions originating from the Γ_7^+ and Γ_8^+ valence bands respectively as is pictured in Fig. 5. Fig. 6 is a typical reflectivity spectrum of a pure crystal. The largest features are due to the 1s states of each of these excitons. Higher energy states of the blue and violet excitons are often very difficult to observe experimentally so that the reflectivity spectrum is dominated by the 1s states.

D. Annealing

Activation Energy

In the annealing process, a crystal is heated until the lattice periodicity is essentially restored. This will occur when we anneal to temperatures sufficient to result in appreciable migration of vacancies and interstitials. This migration is referred to as a hopping process because the migrating atoms hop (or jump) out of one potential well into a neighboring one rather than move like a free particle. The ability to migrate through the crystal is dependent upon the amount of energy necessary for an atom to make a single jump and is called the activation energy, Q. Because vacancy migration is the motion of atoms at lattice sites and interstitial migration results from the motion of interstitial atoms, then vacancies and interstitials usually require different activation energies. One may think of vacancy migration as analogous to a bubble of gas floating through a liquid.

Fig. 5

Energy levels for the blue and violet exciton series in Cu_2O.

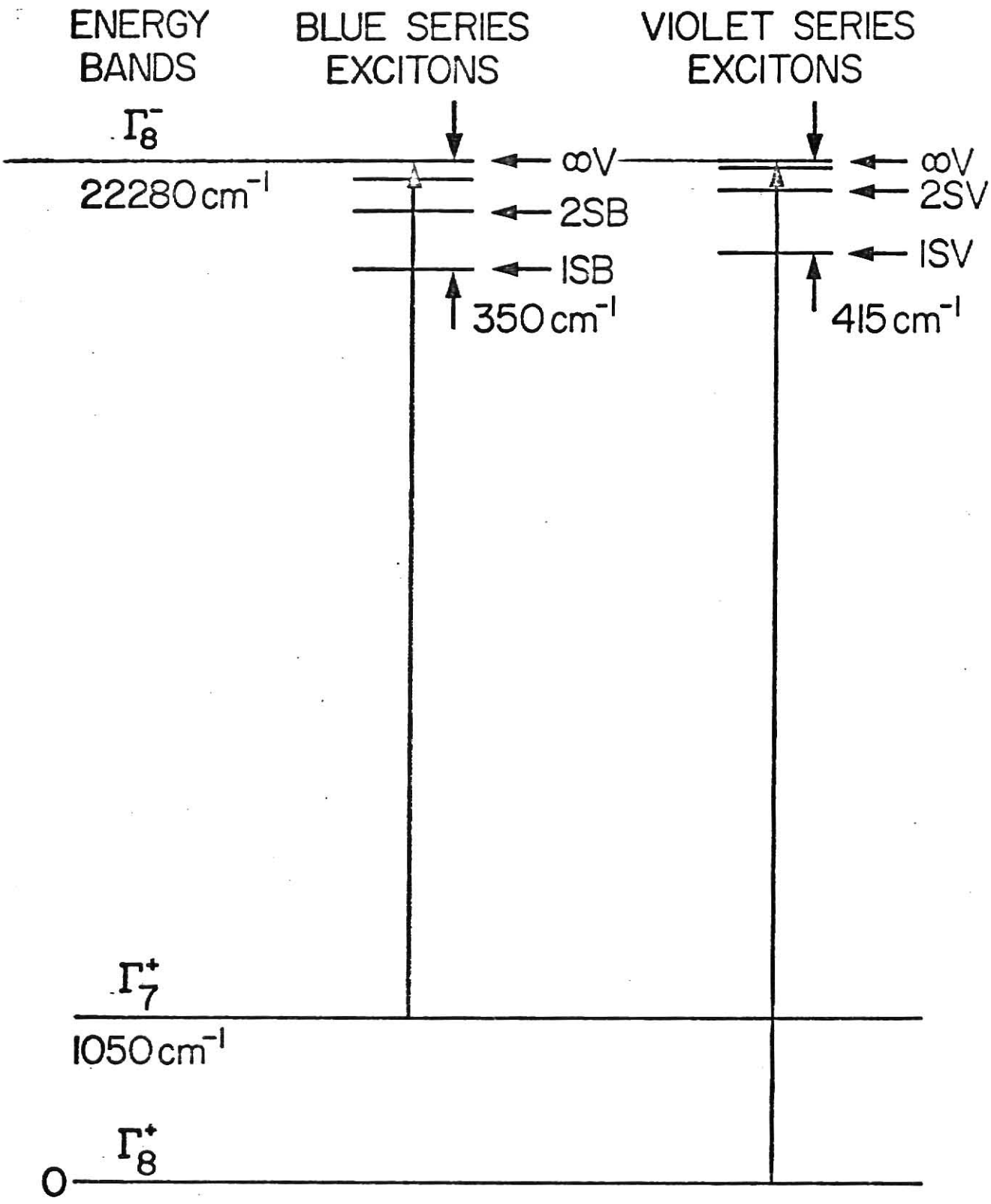
ENERGY BANDS
BLUE SERIES EXCITONS
VIOLET SERIES EXCITONS
Γ_8^-
22280 cm^{-1}
∞V
2SB
1SB
350 cm^{-1}
∞V
2SV
1SV
415 cm^{-1}
Γ_7^+
1050 cm^{-1}
Γ_8^+
0

Fig. 6

Optical reflectivity spectrum for unimplanted, unannealed Cu_2O. The peak in the absorption occurs at the inflection point between the reflectance maximum and minimum for each exciton.


REFLECTANCE (%)
60
50
40
30
20
10
22000
21000
20000
FREQUENCY (cm⁻¹)

The jump frequency, in either case, is the number of hops per second an atom may make during migration. An atom located within any potential well vibrates with a certain frequency. During annealing, the fraction of time[22] the atom has enough energy to surmount the surrounding potential barrier and hop over into the next well is:

$$e^{-Q/kT}$$

so that the jump frequency is:

$$f = \Lambda\, e^{-Q/kT} \qquad 9$$

where k is the Boltzmann constant, T is the temperature during the anneal treatment, Λ is a dimensional parameter equal to the number of nearest interstitial or lattice sites available to the hopping atom. For example, for a vacancy in a simple cubic structure, there are six neighboring atoms, any one of which may hop into the vacancy so that $\Lambda = 6$ in this case.

The activation energy may not be the same for each type of defect and the annealing, in general, will depend upon the time of exposure of the crystal to some temperature T. The activation energy is less for simple defects such as single vacancies and interstitials than it would be for more complex defects such as divacancies and clusters of vacancies and interstitials.[15a] It will also depend upon the size of the diffusing or hopping atoms relative to those which make up the crystal.

The hopping process is a statistical process requiring thermodynamics for a rigorous treatment. The presence of complex defects may block and scatter atoms migrating through the crystal lattice making the entire picture very complicated. For a lattice with little damage, most of the

atoms will probably reoccupy a former site. For a heavily damaged or amorphous region, annealing may result in the formation of a mosaic-like structure of crystallites, each of which is randomly oriented.[15-a]

Anneal Procedures

Two types of anneal procedures are used in the laboratory: 1) isothermal anneals in which the temperature T is the same for each anneal treatment but the length of time the sample is at the temperature T is increased for each successive treatment; 2) isochronal anneals in which the length of each anneal treatment is constant but the anneal temperature T is increased and amount T for each successive treatment.

Isothermal anneals are used to study the temporal dependence of the annealing process whereas isochronal anneals are used to study the temperature range in which the damage most effectively anneals and to determine the activation energy.

E. Luminescence

Luminescence in crystals occurs when an electron in the conduction band recombines with a hole in the valence band and simultaneously creates a photon of energy E. The energy of the emitted photon is generally less than that of the initial photon whose absorption by the crystal resulted in exciting the electron into the conduction band in the first place. Therefore, the observed luminescence occurs at lower energies (Stokes shift) than the band gap energy.

In this section we wish to briefly review several different types of luminescence mechanisms to set the stage for discussion of the extrinsic

luminenscence which has been observed in the Na implanted Cu_2O sample. The subject of luminescence mechanisms is quite extensive so that we will look at some of the more established concepts and highlights. Some of the mechanisms we will look at here are luminescence due to free exciton annihilation, bound exciton annihilation, and free and bound electrons and holes trapping into defects and impurity centers with photon emission.

a. Free electron - free hole recombination

Probably the simplest luminescent mechanism, shown in Fig. 7-1, involves the recombination of a free electron and a free hole. In any collision process, momentum must be conserved. Since the probability is small that a free electron and a free hole will recombine with precisely equal and opposite momenta to form a photon of nearly zero momentum, this type of recombination seldom occurs and the corresponding luminescence is weak.

b. Free exciton annihilation

A second simple case is that of a free exciton which annihilates and emits a photon as shown in Fig. 7-2. The initial state is the free exciton and the final state is the emitted photon which one observes as a sharp peak of energy

$$E = E_g - (m_r^* e^4)/(2h^2E^2n^2) \qquad 10$$

where $m_r^* = (m_{e^-}^* + m_{h^+}^*)/m_{e^-}^* m_{h^+}^*$ is the reduced mass and $m_{e^-}^*$ and $m_{h^+}^*$ are the effective masses of the electron and hole respectively;

Fig. 7

Band transitions for several cases of free and bound electrons and holes involving donor and acceptor energy levels.

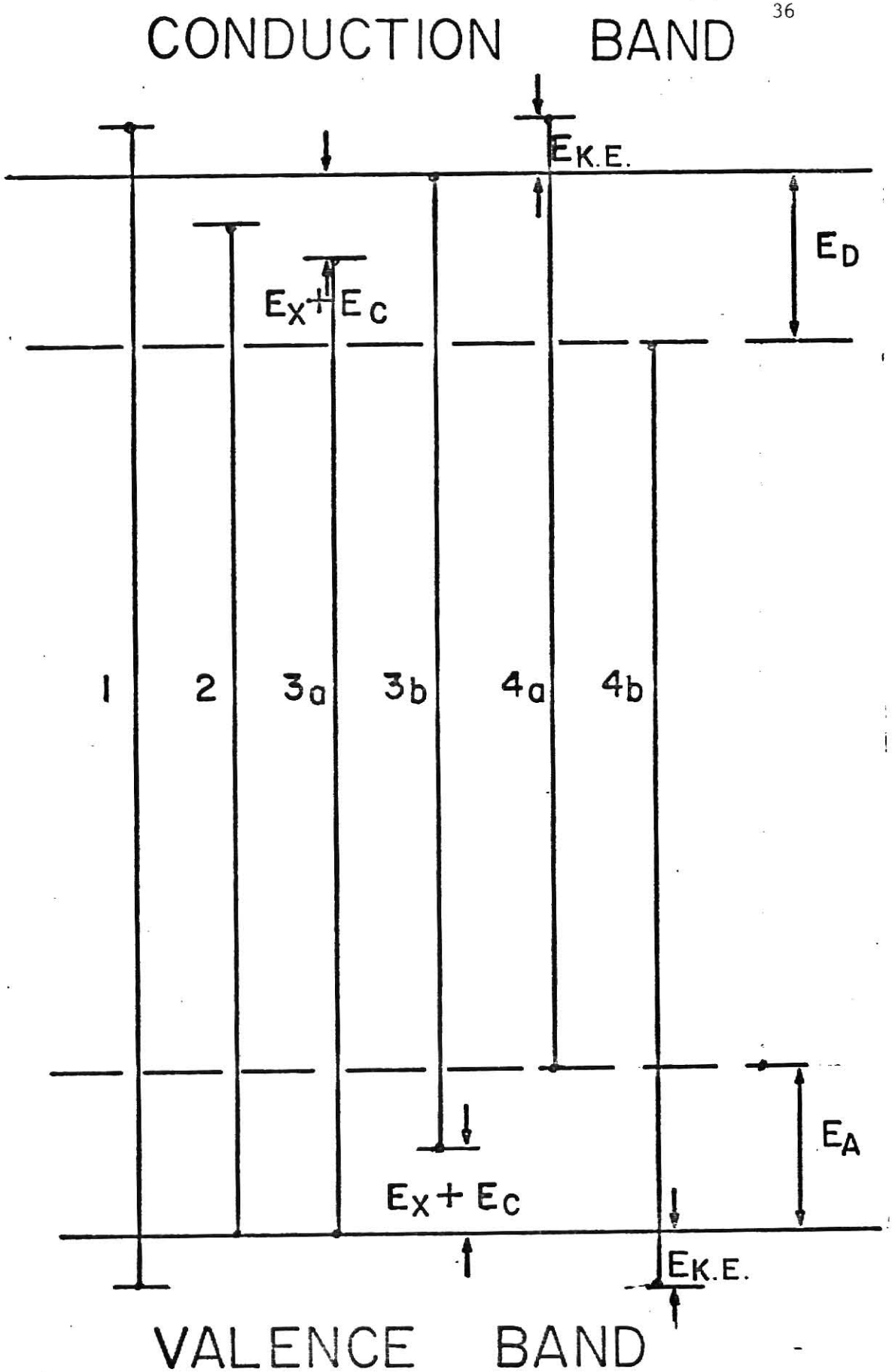
CONDUCTION BAND
$E_{K.E.}$
E_D
$E_X + E_C$
1
2
3a
3b
4a
4b
E_A
$E_X + E_C$
$E_{K.E.}$
VALENCE BAND

$n = 1,2,3,4,....$; E_g is the band gap energy; the last term represents the binding energy of the exciton.

Even these transitions are not easily observed because of momentum conservation. The exciton momentum must be the same as that of the emmitted photon, which is small. Momentum may be conserved, however, with the participation of a lattice phonon in the annihilation process. For this phonon assisted case, a broad luminescence peak appears at an energy lower than the unassisted luminescence energy by an amount equal to the phonon energy. The width of this phonon assisted luminescence is attributed to the kinetic energy of the exciton.

The aforementioned cases generally apply to relatively pure crystals, free from large densities of imperfections. Doped crystals are usually of greater interest in terms of observing additional spectral features due to luminescent mechanisms resulting from the presence of the added impurities.

c. Bound exciton complexes

A bound exciton complex consists of an exciton bound to an ionized donor or acceptor impurity atom. Fig. 7-3a depicts the case for an exciton bound to a donor and Fig. 7-3b depicts the case for an exciton bound to an acceptor. When the bound exciton decays, the emitted photon has an energy of

$$E = E_g - E_x - E_c \qquad 11$$

where E_g is the band gap energy, E_x is the exciton binding energy, and

E_c is the binding energy of the exciton-impurity complex. In this case, one observes sharp spectral features corresponding to the excited levels of the complex which would be shifted to lower energies from the unbound exciton luminescence by an amount equal to the binding energy of the complex.

d. Free - bound transitions

In the free-bound recombination process, a free electron, with kinetic energy kT, in the conduction band becomes bound to an acceptor atom, as shown in Fig. 7-4a. In the process, a photon of energy $E = E_g + kT - E_A$ is observed. The width of the luminescence is kT because of the thermal distribution of the free electrons. We can have a similar process for a hole recombination from the valence band to a donor state.

III. Experimental Setup

A. Sample Preparation

Two separate sets of Cu_2O samples were used in these experiments. The first set of samples were precut to a thickness of 0.4 mm from a large crystal boule which was grown using a floating zone technique[27] and sent to us by R. A. Forman of the National Bureau of Standards. The second set of samples was cut from a different crystal boule also grown using the same technique at the Bureau of Standards. This latter boule was presumably of poorer quality than the boule for the first set of samples because this second boule was actually grown prior to the first boule and before they had refined their crystal growth techniques. We cut several 0.75 mm samples using a diamond blade Buehler Ltd. 11-1180 Low Speed Saw with vacuum pump oil as a cutting lubricant. Saw marks were removed by hand grinding both sides of each sample on #600 grit abrasive paper. These samples were polished with 1.0 μm aluminum oxide (Al_2O_3) polish mixed with distilled water for one-half hour on a felt pad. Little change occurred in the surface appearance of this second set of samples with an additional 10 minutes of polishing using 0.3 μm Al_2O_3. The second set of samples had large numbers of inclusions after polishing, indicative of their poor quality. Both sets of samples subsequently, were wiped clean with acetone and then chemically etched in concentrated nitric acid for 30 seconds in order to remove the damage layers due to the mechanical polishing[1] described earlier. While in the nitric acid, the samples must be kept in a constant circular motion

parallel to the plane of the sample surface in order to etch them as evenly as possible and to assure all the samples of a given set were prepared in the same way. After being chemically etched, the samples need to be washed immediately with clean distilled water to stop the etching process. The samples must be swished in the water, otherwise acid films may continue to etch the Cu_2O unevenly. After the water wash, the samples are dried thoroughly to avoid water marks. A final wipe with acetone completed the pre-implantation sample preparation.

The samples of the first set (0.4 mm thick) were labeled "a" through "h". The second set of samples (0.75 mm thick, and presumably of poorer quality) were labeled "3" through "11".

B. Ion Implantation

The ion implantation was performed on the 100 keV accelerator of J. R. MacDonald at Kansas State University. A schematic of the accelerator is shown in Fig. 8. The isotope separation and collimating of the beam was achieved by an analyzing magnet in conjunction with various apertures and is capable of isolating single isotopic beams. A Hall probe monitored the magnetic field and was calibrated to the field necessary to select out an argon ion beam of mass 40. The resolution of the system is 2 mass units out of 100 so that contamination of the ion beam was not a major concern.

The target-sample holder is illustrated in Fig. 9. Consisting mainly of a stainless steel mask with 4 holes, 3 samples, one behind each of 3 holes, are mounted on the middle plate with Eccotherm TC-4 white thermal paste and copper wire clips. The fourth space remained

Fig. 8

Ion implantation apparatus.

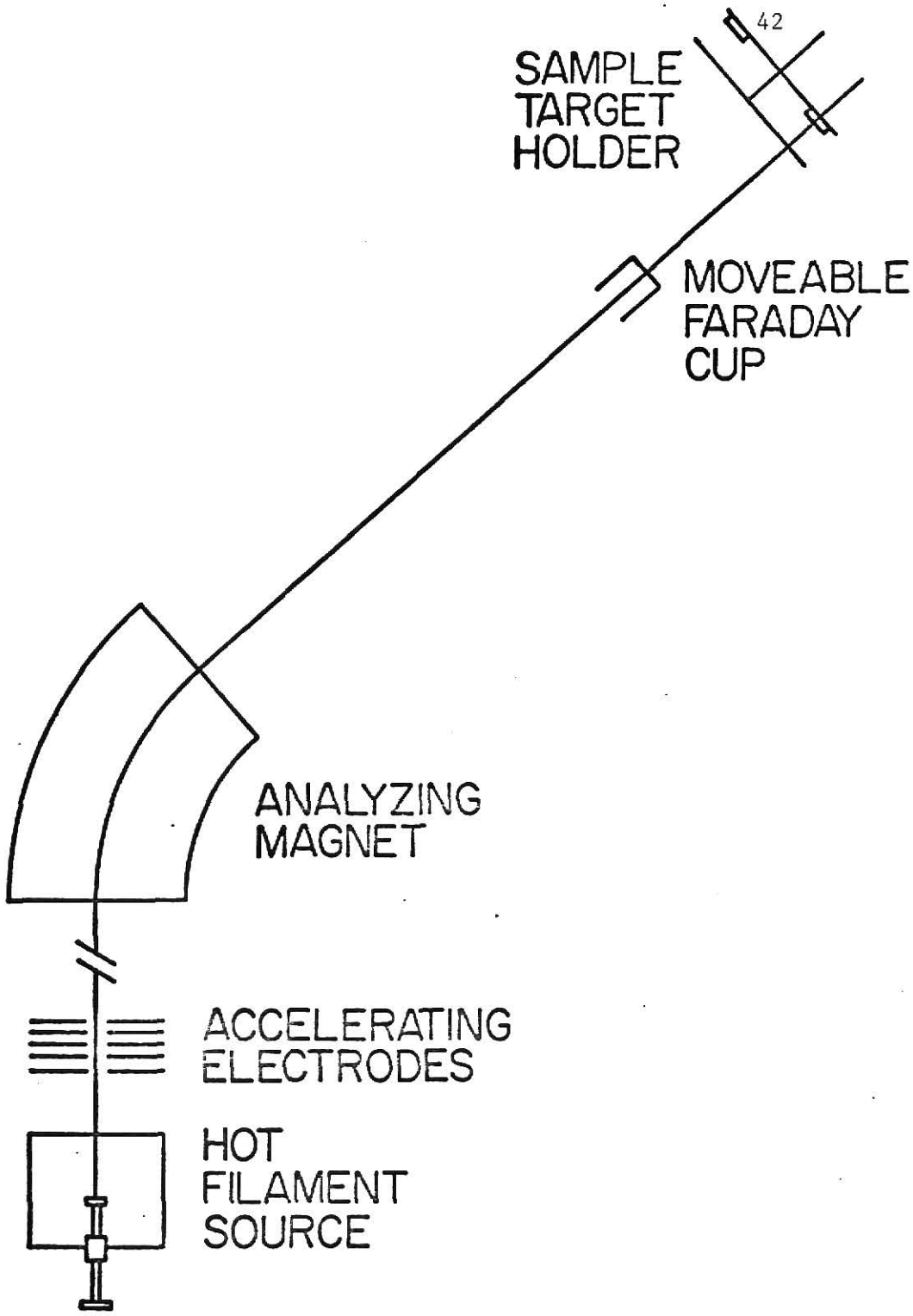

IMPLANTATION SET-UP

Fig. 9

Target sample holder. Holds up to four samples.

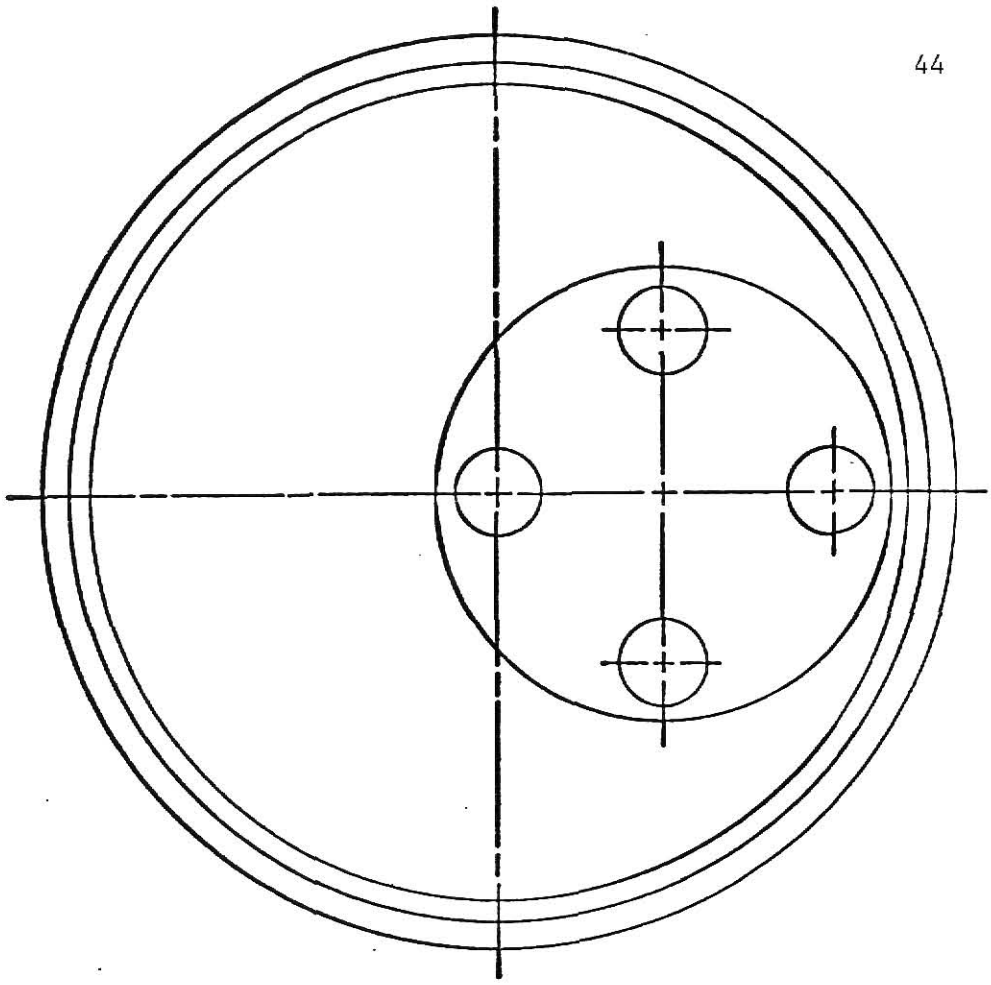

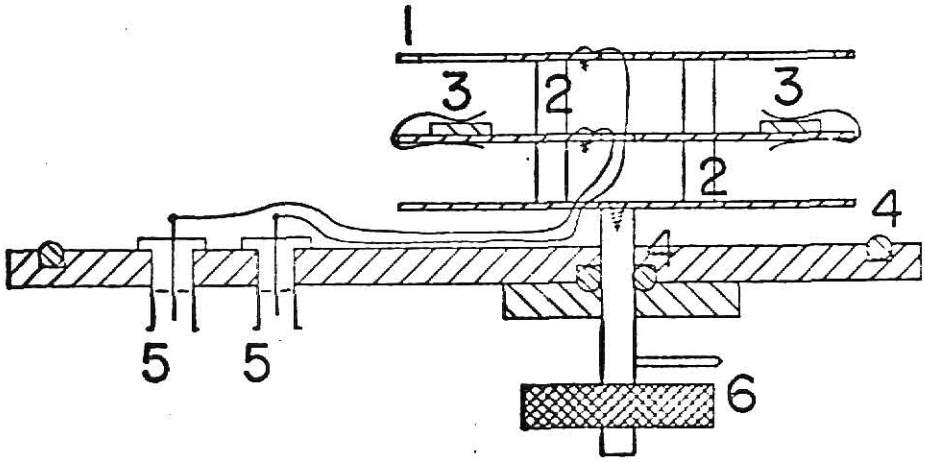

1 MASK WITH HOLES
2 INSULATING POST
3 Cu_2O SAMPLE
4 "O" RING
5 CONNECTORS FOR ION CURRENT MONITORS
6 SAMPLE SELECTOR WITH POINTER

TARGET HOLDER SCHEMATIC

vacant for purposes of fine alignment of the ion beam onto the target sample holder. The ion beam was adjusted until the current is maximized on the middle plate at the vacant spot and is minimized on the mask (that is, most of the beam passes through the hole in the mask). A Faraday cup, inserted into the path of the beam in front of the target-sample holder, measures the total beam current. Once the alignment was made, the beam was blocked by a small slab of quartz glass which doubles as a visual monitor since the quartz flouresces when excited by the incident ion beam. The target-sample holder was rotated until a sample is in the path of the ion beam. The quartz slab was then removed for a sufficient period of time until the desired ion dose is acquired in the sample.

For the first set of samples, the integrated current was continuously monitored until the charge accumulated to the desired level. The doses for the second set of samples were controlled by monitoring the current for a predetermined length of time until the desired charge was obtained. With a mask aperture of area 0.2 cm^2, we may compute the ion dose. For example, a Ag^+ current of .15 μA on the sample for 18 seconds gives a dose of:

$$.15 \times 10^{-6} \frac{\text{Coul}}{\text{Sec.}} \times 18 \text{ sec.} \times \frac{1 \text{ ion}}{1.6 \times 10^{-19} \text{Coul}} \times \frac{1}{0.2 \text{ cm}^2} = .84 \times 10^{14} \frac{\text{ions}}{\text{cm}^2}$$

The first set of samples (labeled a - h) are listed in Table I with some implantation data. Table II lists this data for the second set of samples (labeled 3 - 11).

Table I

Implantation data for 1st set of Cu_2O samples.

SAMPLE	ION SPECIE	ENERGY (keV)	CURRENT (μA)	TIME (SEC.)	CHARGE (μC)	DOSE (IONS/cm^2)
A	Cd^{++}	184	~0.01	~720	7.27	10^{14}
B	Cd^{++}	184	–	–	0.0008	10^{10}
C	Cd^{++}	184	0.01	720	7.2	10^{14}
D	Cd^{++}	184	0.01	720	7.2	10^{14}
E	Cd^{++}	184	0.0092	780	7.21	10^{14}
F	Cd^{++}	184	0.0158	~60	0.95	2×10^{13}
G	Cd^{++}	184	0.01	720	7.2	10^{14}
H	Cd^{++}	184	~0.01	~720	7.18	10^{14}

Table II

Implantation data for 2nd set of Cu_2O samples.

SAMPLE	ION SPECIE	ENERGY (keV)	CURRENT (μA)	TIME (SEC.)	CHARGE (μC)	DOSE ($\times 10^{14}$ IONS/cm^2)
3	Ag^+	60	0.150	18	2.7	0.84
4	Na^+	92	3	6	18	5.6
5	Ag^+	60	0.040	6	0.24	.074
6	Na^+	92	3	60	180	56
7	Na^+	92	0.1	6	0.6	0.18
8	Ag^+	60	0.150	18	2.7	0.84
9	He^+	60	0.70	540	378	117.6
10	He^+	60	0.080 — 14 0.350 — 4		2.5	0.77
11	He^+	60	1.2	72	63.4	19.7

In measuring the ion current, one needs to be careful since the total current of the ion beam may be less than the sum of the currents measured on the mask and on the middle plate-sample holder. The increase is due primarily to secondary electron emission. Secondary electron emission occurs when a charged particle excites electrons of the solid being irradiated and ejects them completely out of the solid. Electrons leaving the solid effectively increases the current measured. On the average, less than one electron per incident charged particle is emitted for a beam of electrons of 10 keV or greater.[28] For ions, the number of ejected electrons is probably not any greater. Otherwise correction factors, to be discussed below, would be much smaller than they actually are. One method of correcting for secondary electron emission is to assure that they do not escape the sample in the first place. This is achieved by applying a suppression voltage at certain places in the target apparatus, depending upon the geometry of the apparatus (this is the principle of the Faraday cup). If this is not done, an alternative is to simply correct the current measurements. We are interested in the true ion current on the target and the mask, I_t and I_m respectively. The ion beam current is

$$I_b = I_t + I_m$$

we assume that

$$I_b = \gamma \times I \qquad 12$$

where γ is a factor determined experimentally, and I is the total measured current,

$$I = I_t' + I_m' \qquad 13$$

I_t' is the measured target current, and I_m' is the measured mask current. We then write

$$I_t = \gamma_\delta \times I_t'$$
$$I_m = \gamma_\delta \times I_m' \qquad 14$$

where $\gamma = I_b/I$. Typically, $\gamma_\delta = 1.1/1.5 = 0.73$. I_b is generally measured with a Faraday cup. Multiplying by γ_δ corrects for the secondary electron emission.

C. Sample Mounting for Raman Scattering Experiments

Several different sample mounting techniques were used during these experiments. Each succeding technique had some advantages over its predecessor. The samples were mounted onto a copper sample holder. Initially, "Eccotherm TC-4" white thermal paste was used to attach the samples to the copper sample holder. This paste gave adequate thermal contact and did not strain the sample when cooled, however, it was difficult to completely clean off for the purpose of annealing the sample. A second technique that was used did an excellent job of keeping the samples clean for annealing. Here we held the samples on with copper wire clips. However, good thermal contact was inadequate. The third technique we used combined easy sample cleaning for anneal purposes with good thermal contact. Here we used "G. E. 7031" low temperature varnish. This is a standard sample mounting adhesive and generally binds the sample tightly when care is taken to assure both the sample and holder are clean and free of grease and oxide films (copper tarnishes easily).

Also, roughening the backside of the sample increases the area of contact which improves the thermal contact. We generally let the varnish dry overnight. The excessive use of this varnish leads to problems. If the entire backside of the sample is covered with the varnish and if it binds tightly, differences in the thermal coefficient of expansion between the sample and the copper sample holder will excessively strain the crystal so that it fractures when cooled to 80 K. Not only does the good single crystal suddenly become a number of small fragments and the implanted region now becomes several, but the fracturing may destroy the good thermal contact present prior to the break. The solution to the problem seems to be to use only tiny amounts of the varnish and apply only behind the region of interest of the crystal.

The sample holder was inserted into the brass tube cold finger of a pyrex glass liquid nitrogen dewar constructed by M. Ohno of Kansas State University. The inserted end of the holder was coated with Air Products "Crycon Grease" and held stationary by a pair of teflon set screws for good thermal contact. A copper-constantan thermocouple was attached to the backside of the sample holder to monitor its temperature. An accurate measure of the temperature of the irradiated portion of the sample is obtained by looking at the position and intensity of the phonon assisted luminescence of the 1s "yellow" exciton. At a temperature of 77 K, the edge of the Stokes side is at 16, 225 cm^{-1}. The edge shifts approximately 2 cm^{-1} per degree Kelvin in the vicinity of 50 - 200 K.[29] The Stokes edge occurs at 109 cm^{-1} from the zero phonon peak since it is the 109 cm^{-1} phonon which assists in the decay of the exciton. Another way to check the

sample temperature is to look at the Stokes-Anti Stokes ratio of the phonon assisted sideband intensities:

$$I_S/I_{AS} = (n + 1)/n = e^{\frac{hc}{kT}} \qquad 15$$

where n is the phonon population factor, $n = 1/(e^{\frac{hc}{kT}} - 1)$

Solving for the temperature T:

$$T = \frac{hc}{k} \quad \frac{1}{\ln(I_S/I_{AS})} \qquad 16$$

where h = Planck's Constant, c = Speed of light; = 109 cm^{-1};

k = Boltzmann Constant.

For example, from Fig. 10 we have a typical spectrum of the phonon assisted luminescence of the 1s "yellow" exciton. The zero phonon peak is marked by an arrow. After subracting out the background under each peak (dashed line), we measure I_S and I_{AS} and find:

$$I_S/I_{AS} = 6.17$$

plugging into the expression for T we get:

$$T = \frac{(6.63)(3)(1.09) \times 10^{-22}}{(1.38)(\ln(6.17)) \times 10^{-23}} = 86 \text{ K}$$

If the observed edge is near 16,200 cm^{-1}, then the temperature of the irradiated portion is probably within $\pm$ 5 K of 86 K computed above. This temperature will vary some, depending upon the quality of the binding and thermal contact. The effects of temperature variations on the Raman intensities depends on the Raman feature of interest. From the phonon population factor, n, it can be shown that the intensity of the 154 cm^{-1} Stokes Raman feature, for example, will vary by less than 1% between 80 and 85 K. The 154 cm^{-1} Anti Stokes feature, however, will change by ~16% between the extremes of this temperature range.

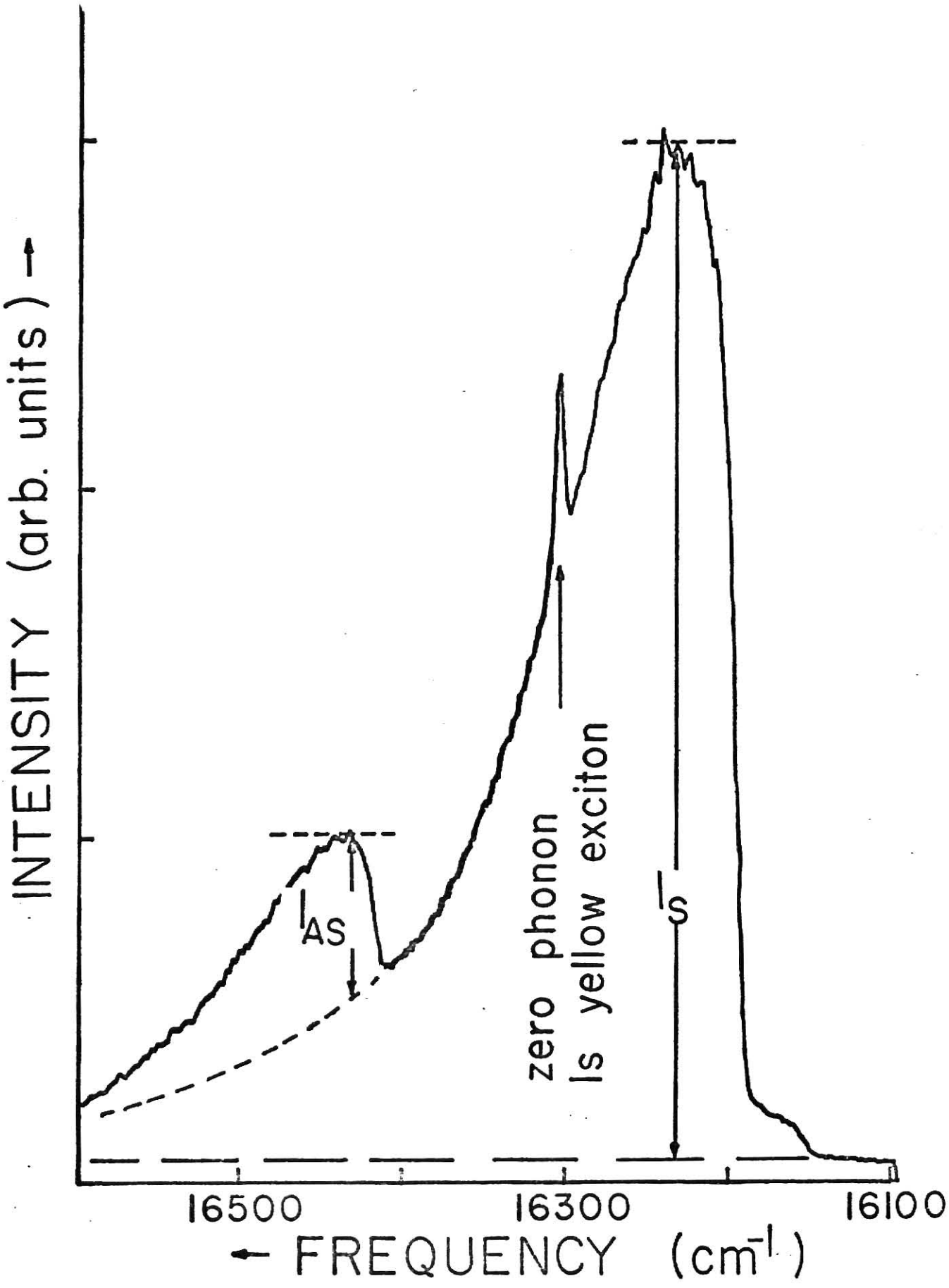
INTENSITY (arb. units) →
AS
S
zero phonon
Is yellow exciton
16500
16300
16100
← FREQUENCY (cm⁻¹)

D. Raman Scattering

Figure 11 illustrates the Raman scattering experimental setup. Laser excitation from a Coherent Radiation Model 52 Argon Ion Laser is incident upon the sample at an angle of $\sim 8°$ as is defined in Figure 12. The incident light is polarized in the plane of incidence and the Raman scattered light is of mixed polarization in general. The Raman scattered light is collected at 90° relative to the incident beam direction and is focused onto the entrance slit of a Spex Model 1401 Double Monochromater. The double monochromator has 3 slits: the entrance slit is set at 0.3 mm; the exit slit which is located prior to the photomultiplier tube and is set also at 0.3 mm; and finally an intermediate slit set at 0.4 mm and which is located between the two reflective gratings in the instrument. The resolution of the spectrometer for the above slit settings is 8.8 cm^{-1} when using light whose wavelength is 476.5 nm.

The Spex is stepped in increments of 2 cm^{-1} for purposes of obtaining digital data. The photons were detected by a thermoelectrically cooled ITT FW-30 photomultiplier tube containing an S-20 cathode. The output consisted of pulses which were counted for 2 seconds by electronics constructed in this laboratory[30] and consisting basically of a preamp, and amplifier, and a discriminator. The total number of pulses counted is displayed on a digital readout of a Hewlett-Packard 5326C Frequency Counter and whose output is fed to a digital paper tape punch to record the data.

The power of the incident Laser excitation was checked periodically for stability by a Scientech Model 3600 Disc Calorimeter. The laser output

Fig. 11

Raman scattering and photon detection system.

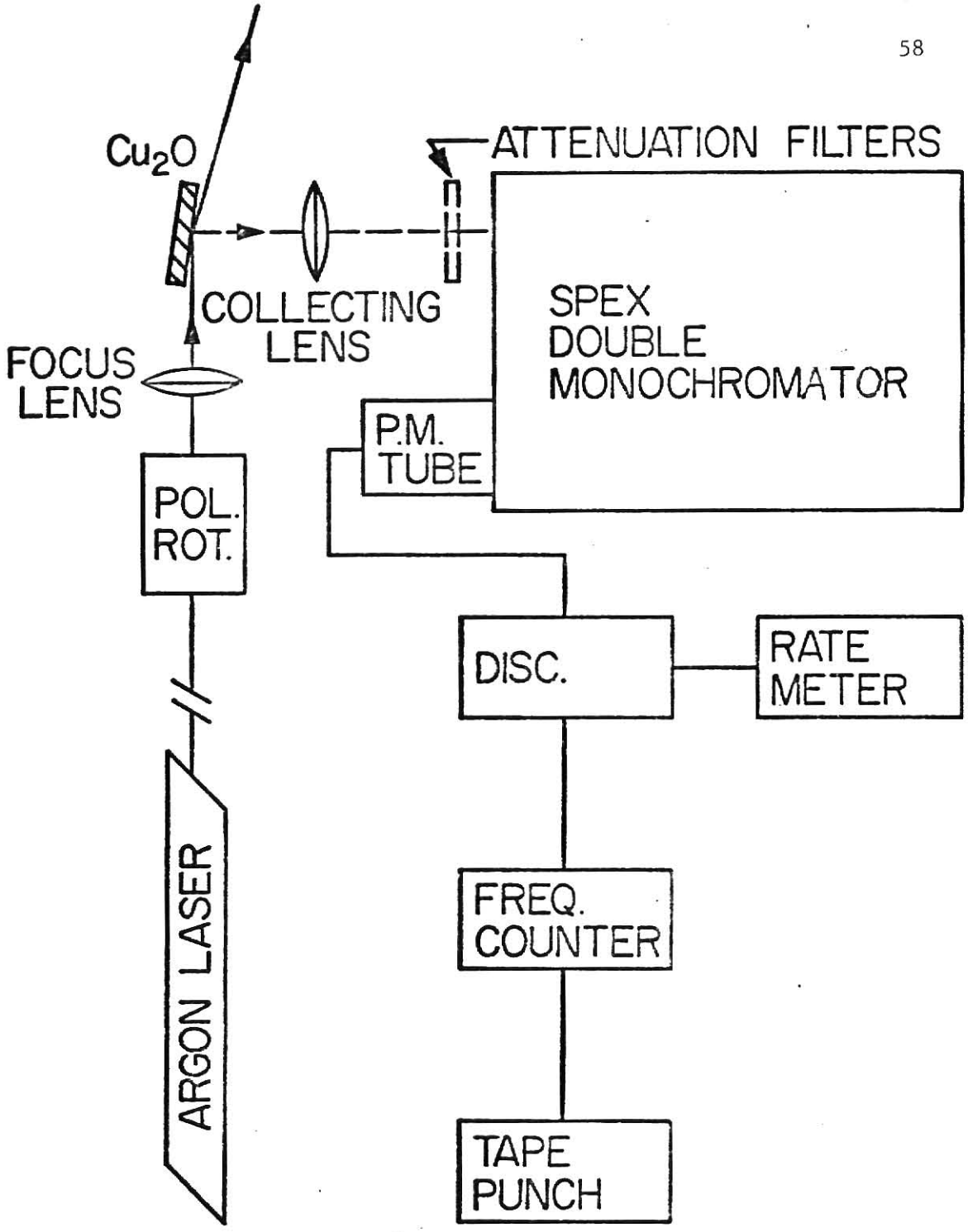

RAMAN APPARATUS

Fig. 12

Raman scattering geometry.

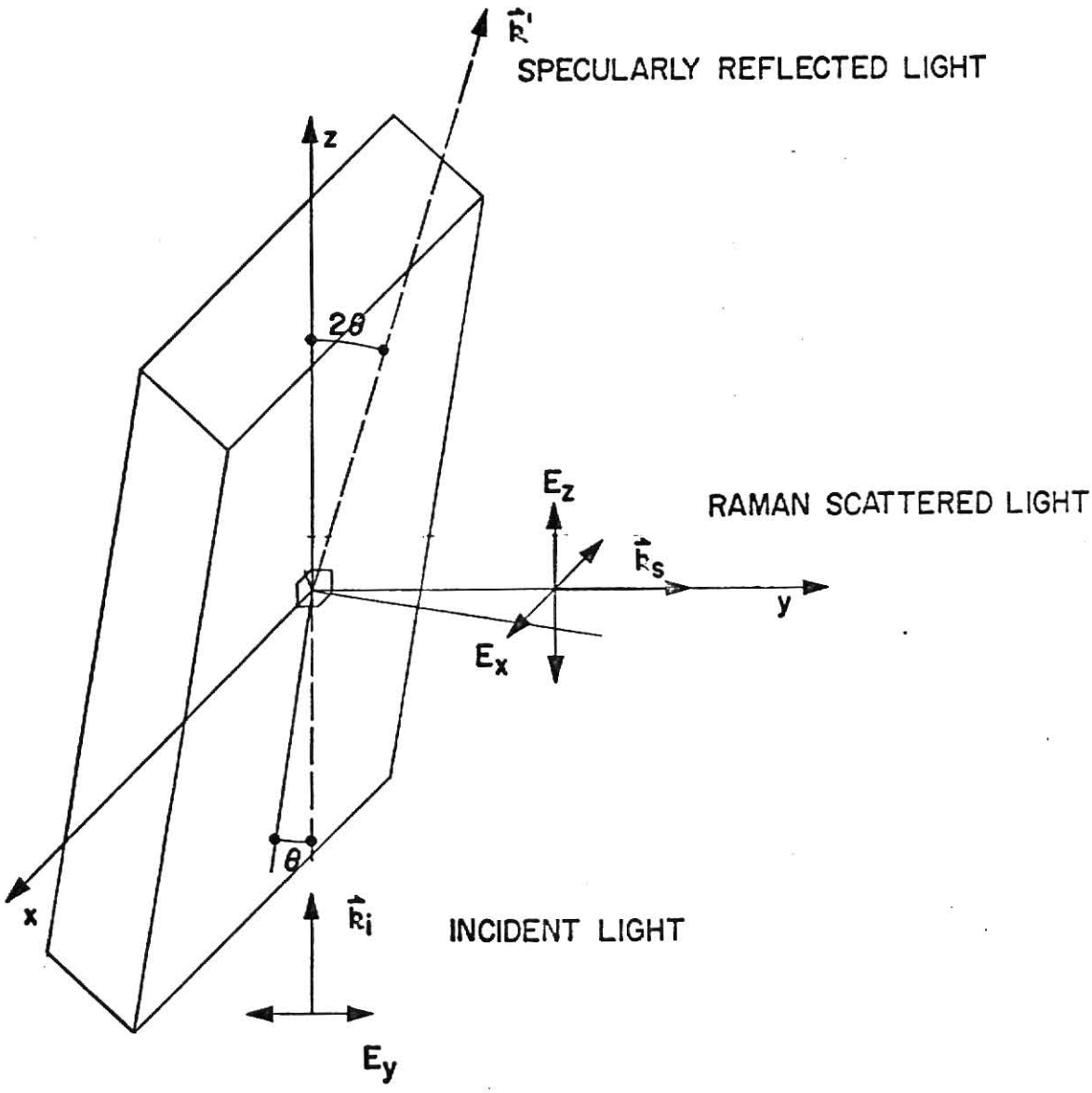

RAMAN SCATTERING GEOMETRY

was also continuously monitored by a system in which a glass microscope slide picked off a fraction of the laser light and deflected it onto a photovoltaic cell (not shown) which displayed the power in terms of a current. The stability of the observed current was indicative of the stability of the laser. A series of neutral density filters was necessary to attenuate the collected Raman scattered light by factors of 10^6-- 10^8 to protect the photomultiplier tube when the spectrometer scanned past the laser frequency. The filters were removed within 50 cm^{-1} of the laser peak when the scattered light reached safe levels. At the end of each spectrum, the spectrometer was scanned back to a Raman line near the beginning (generally the 150 cm^{-1} feature) to compare its present intensity with its intensity the first time scanned through in order to check on any possible drifting and sample movement.

E. Optical Reflectivity

The system for the optical reflectivity experiment is illustrated in Fig. 13. Initially we attempted to use a split beam geometry in conjunction with standard electronics consisting of a Molectron model #122 Dual-Gate Generator, a Molectron model #112 Differential Gated Integrator, and a Molectron model #151 Multiplier/Divider. Problems of the zero point drifting in the integrators independently of each other made this system unreliable.

Two different systems were subsequently used. In the first system, we employed a split beam geometry, one initial beam split into 2 beams by a partially silvered glass plate. One beam was reflected off the implanted region of the sample (sample beam) and directed into the

Fig. 13

Optical reflectivity and photon detection system.

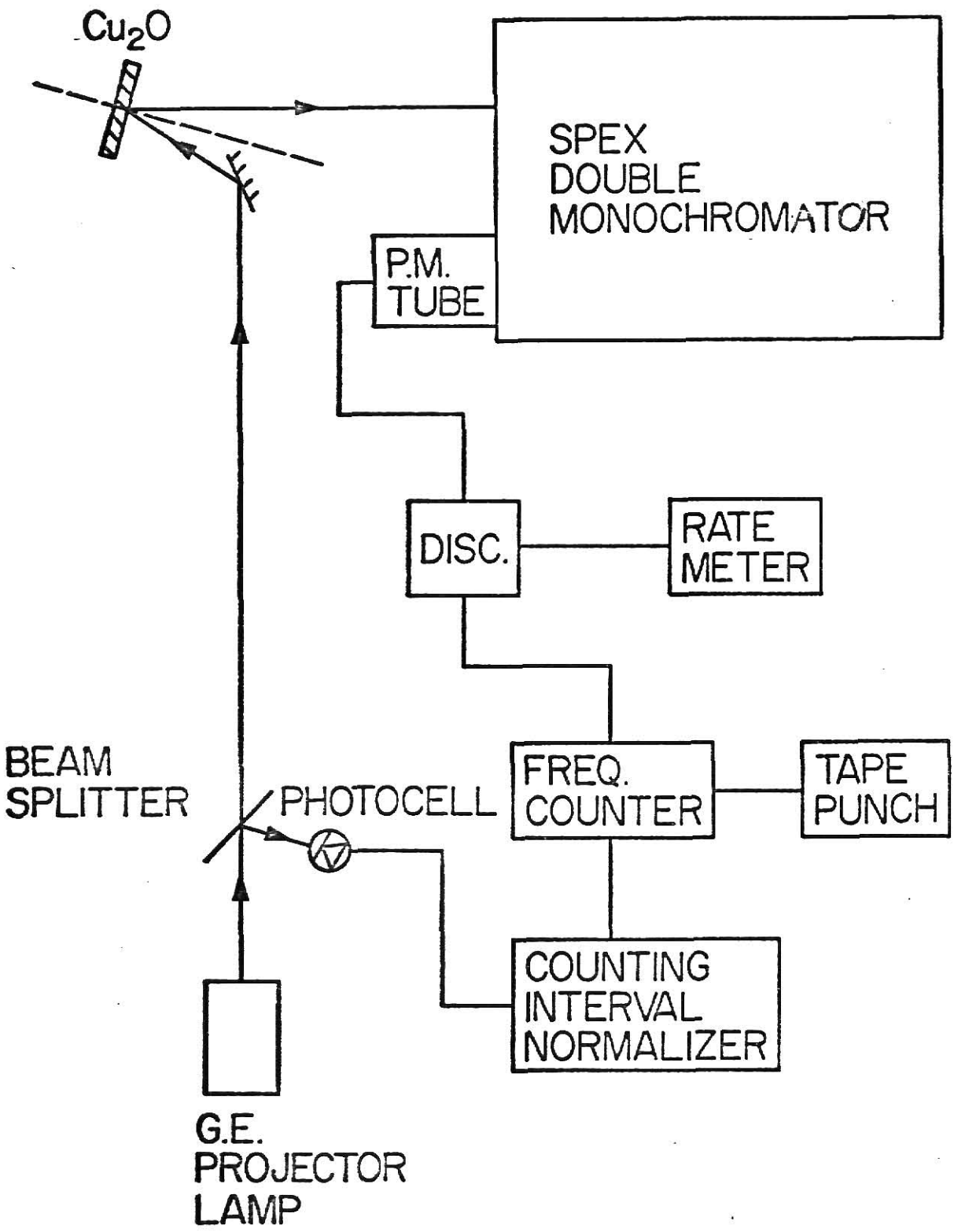

OPTICAL REFLECTIVITY APPARATUS

spectrometer. The other portion was reflected off a reference mirror located above the sample and also attached to the sample holder. This beam (reference beam) was also directed into the spectrometer. With this set up, it was necessary to manually alternate the two beams by blocking one, then the other with a card while the photon detection system (same as that used for the Raman experiment) counted and advanced the spectrometer. The result was that every other point on the digital readout (papertape punch) was for the sample and the points in between were for the reference. A program for the Hewlett-Packard 9100 B calculator would select every two data points on the papertape, divide the sample data point by the reference data point, normalize it to a chosen reflectance (to be explained later) to give us the percent reflectivity. This method worked fairly well. Because of the tediousness of the data taking process (taking a data point every 5 cm^{-1} for a period of 4 seconds and covering a spectral band of 4,000 cm^{-1} required a time of ~53 minutes) an alternative process was worked out.

In the second system, shown in Fig. 13, we did not split or chop the beam because of the use of a system of electronics called "Counting Internal Normalizer" (CIN).[30] In the system described above, we alternated the beams immediately to minimize effects of source fluctuations since any possible fluctuations were assumed to be long term. With the CIN system, a portion of the incident light onto the sample is picked off and directed onto a photovoltaic device. The resultant current is fed into the CIN which, because of the amplitude of the signal, counts for a certain length of time. If the reference signal increases or decreases by a factor

of m, then the length of counting time decreases or increases by a factor of m respectively. This system would account for fluctuations in the source and because of the single beam, is easier to align with the spectrometer than the split beam. Because of the greater intensity obtained, the statistics of the experiment were improved in addition to less time to take data and freeing the experimenter for other duties. Also, a reference scan need only be taken once. Now the sample data is on a separate paper tape than the reference data so that we rewrote the ratio program for our plotting system. The use of the Hewlett-Packard (H-P) 9101 A Extended Memory would store a part of the data from one tape while the calculator would then read a data point from the other tape and combine it with a data point corresponding to the same spectral position of the spectrometer, read out of the Extended Memory and then plot the percent reflectivity. The sample system was checked for drift and motion in an identical manner as for the Raman experiment.

IV. Data and Results

A. Reflectivity Data

The behavior of the optical reflectivity spectra with annealing of implantation-produced damage is important in order to understand the behavior of the phonon Raman spectra. This is important because in the case of Resonance Raman scattering, the scattered photons are resonant with intrinsic exciton states. These states are real electronic states which "replace" the virtual electron-hole states occuring in the non-resonant case. Figures 14 and 15 show composites of the reflectivity of Cu_2O illustrating the annealing behavior of the violet exciton (21,900 cm^{-1}) and the blue exciton (20,850 cm^{-1}) series. Trace "a" of each figure displays the reflectivity of an unimplanted corner of the crystal. The data shown here has been normalized to 30% reflectance at 23,000 cm^{-1} based on the reflectivity spectrum of reference 31. This normalization was necessary because we had no built in reference. We therefore assumed the reflectivity at 23,000 cm^{-1} remains constant during the annealing. The result of the normalization is to provide the same reference point for each spectrum necessary for comparison purposes.

Several important features of the data are noted here: i) the nearly complete smoothing out of the reflectivity in the implanted, unannealed sample as indicated in trace "b" of Figures 14 and 15; ii) the gradual recovery of the exciton features during series of anneal treatments; iii) the narrowing of the features as measured between the minimum and maximum reflectance for each exciton; iv) a shift to lower energy of the reflectivity minimum of each feature, with the introduction

Fig. 14

Reflectivity spectra for the Cd^{++} implanted cuprous oxide ("h") illustrating the annealing behavior for a series of 30 minute isochronal anneal treatments: a) unimplanted edge; b) 27°C; c) 250°C; d) 270°C; e) 350°C; f) 390°C. The various spectra are displaced vertically for convenience. Each trace is normalized to 30% reflectivity at 23,000 cm^{-1} (see text).

Fig. 14

Reflectivity spectra for the Cd^{++} implanted cuprous oxide ("h") illustrating the annealing behavior for a series of 30 minute isochronal anneal treatments: a) unimplanted edge; b) 27°C; c) 250°C; d) 270°C; e) 350°C; f) 390°C. The various spectra are displaced vertically for convenience. Each trace is normalized to 30% reflectivity at 23,000 cm^{-1} (see text).

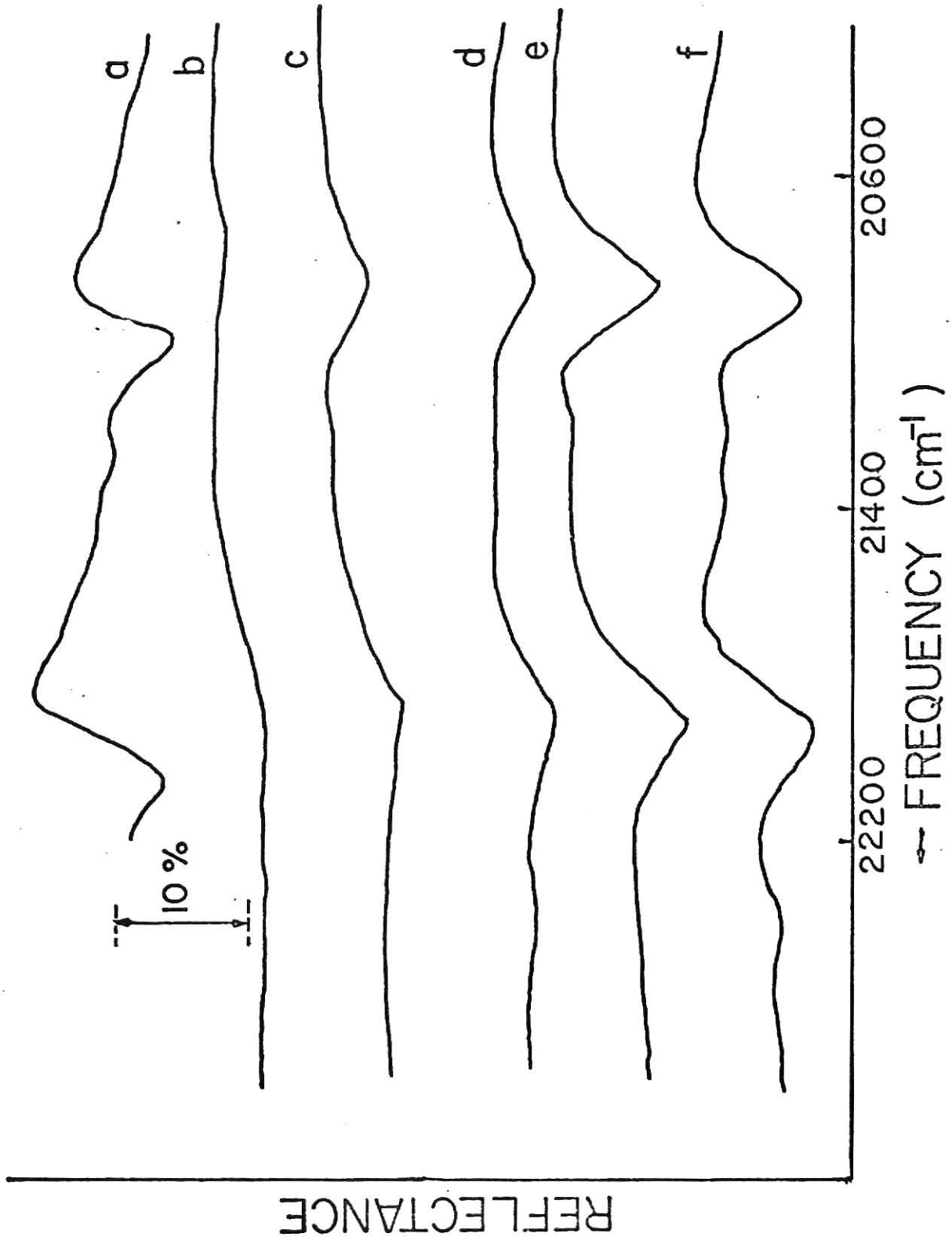
a
b
c
d
e
f
10 %
22200
21400
20600
FREQUENCY (cm⁻¹)
REFLECTANCE

Fig. 15

Reflectivity spectra for the He^+ implanted cuprous oxide ("9") illustrating the annealing behavior for a series of 60 minute isochronal anneal treatments: a) unimplanted edge; b) 190°C; c) 230°C; d) 270°C.

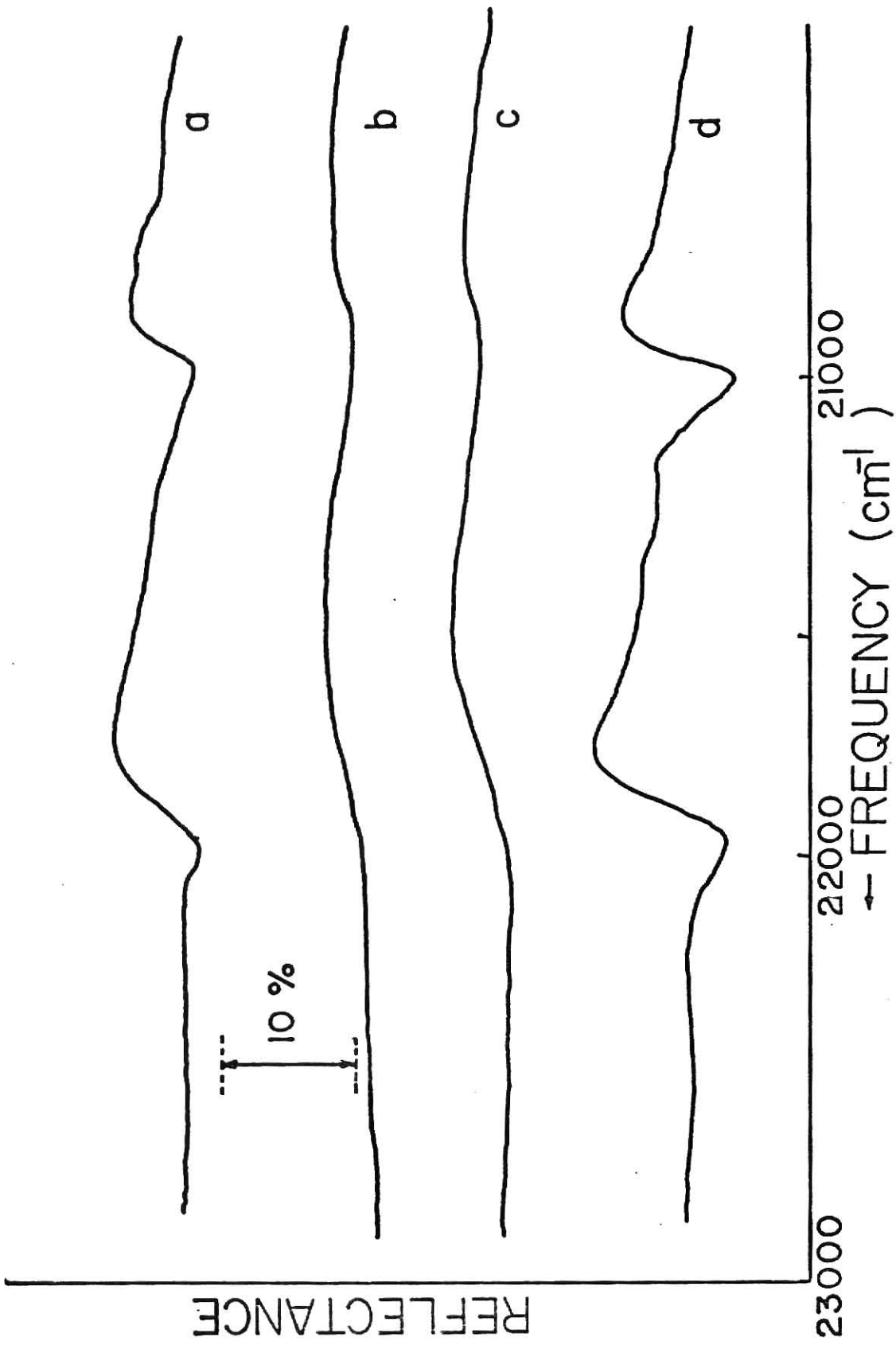
a
b
c
d
10 %
REFLECTANCE
23000
22000
21000
← FREQUENCY (cm⁻¹)

of damage, and its gradual reshift to higher energies as the damage anneals. Table III summarizes the changes in some of the reflectivity data for the Cd^{++} implanted sample.

Exciton energy states result from consideration of the coulomb attraction between an electron of the conduction band and a hole of the valence band in the band theory.[32, 33] With the loss of this periodicity when the lattice is damaged, the exciton states become considerably broadened to the extent that they are no longer distinguishable from the background reflectivity. This data suggests that it is not possible for excitons to exist in material made amorphous by ion implantation.

The broadening of the exciton states may be attributed to two mechanisms: i) the natural width ( ) increases as the exciton lifetime decreases since the excitons in a damaged lattice will scatter from damage sites and impurity centers causing the premature recombination of the electron and hole; ii) damage and impurities induce perturbations in the exciton energy levels. The loss of the periodicity of the lattice perturbs the local potential at each lattice site resulting in broadening of the exciton energies. The relative contribution of each of these mechanisms to the damage induced broadening is not clear.

During annealing, local perturbations due to damage sites disappear as the lattice order is restored. The exciton features reappear and narrow in width, approaching those of a nearly perfect lattice, as the exciton lifetimes again increase because of less scattering from damage sites. Depending upon the type of ion implanted, some broadening will remain if the ions occupy lattice and/or interstitial sites rather than anneal out.

Table III

Reflectivity data for Cd^{++} implanted, annealed Cu_2O sample.

SAMPLE "h"			
ANNEAL TEMP. (°C)	WIDTH (cm^{-1})	Δ%: PEAK-VALLEY	POSITION OF INFLECTION POINT (cm^{-1})
270	326	3.7	20,709
350	253	7.8	20,757
390	216	8.3	20,792
UNIMPLANTED EDGE	123	8.7	20,890

From Fig. 15, the reflectivity for the He^+ implant appears to have annealed quite completely. From this, it is apparent that the He ions have annealed out. This seems reasonable because He is an inert gas so it does not form compounds readily. Also He is a light atom and should diffuse rather easily. Fig. 14, on the other hand, indicates that either Cd ions remained in the Cu_2O or else higher orders of damage exists such as divacancies and vacancy-interstitial clusters. These higher orders of damage would require higher anneal temperatures than those used. These large defects would produce strains probably indistinguishable from those due to the presence of the Cd ions. Strains due to the presence of the Cd ions and other defects would probably consist of both increases and decreases in the lattice spicing with the net result being a broadening if the exciton states. The apparent shift of the minimum in the reflectivity for the Cd implant cannot be readily explained on the basis of changes in lattice constants nor with the data at hand since the exciton states cannot be clearly defined.

Though the He^+ implanted sample (Figure 15) appears to have annealed rather completely, we must consider the fact that the He^+ ion dose is 100 times higher than the Cd^{++} ion dose (Figure 14). Fig. 1 tells us that the value of S_n for 90 keV He into Cu_2O is 200 - 300 times lower than the S_n for 184 keV Cd^{++} into Cu_2O. Therefore, the damage density for the Cd ion is probably 2 - 3 times greater than that for the He ion. Though this implies the damage is not a great deal heavier, the Cd ions probably produce more complex types of damage as stated earlier.

B. Raman Data

Cu_2O has six atoms per unit cell, and therefore, displays a rather rich phonon Raman spectrum. This spectrum, illustrated in Fig. 16 for 476.5 nm excitation, consists of one Raman allowed mode (515 cm^{-1}), two infrared active modes (154 cm^{-1}, 635 cm^{-1} and 665 cm^{-1}), a mode neither infrared or Raman active (109 cm^{-1}), two second order modes (218 cm^{-1}, 308 cm^{-1}), a second order combination (820 cm^{-1}), and a fourth order mode (436 cm^{-1}).[2] Fig. 16 is an ion dose dependence study by Powell, *et al.*[2] *from this laboratory. It shall be used in* this thesis for illustrative purposes and for damage-estimate comparisons later.

Argon ion laser excitation of 476.5 nm and 488.0 nm are used because of their near resonance with the 1s blue exciton (20,850 cm^{-1}, 80 K) of Cu_2O. As is illustrated in the absorption curve for pure crystal Cu_2O shown in Fig. 17, the 476.5 nm (20,986 cm^{-1}) excitation is almost in resonance with the 1s blue excitation, the two being separated by 140 cm^{-1}. In this case the laser frequency lies between the 1s and 2s excitonic states and the phonon Raman Stokes scattered photons whose energies lie within 100 cm^{-1} of the 1s state absorption peak will generally be of high intensity relative to those scattered photon frequencies further away. (This is called "out resonance" because the scattered photons are in resonance with the 1s blue exciton state. For 488.0 nm (20,490 cm^{-1}) excitation, the incident photon is 360 cm^{-1} away from the 1s blue exciton state in the direction of lower energy. Here much less resonance enhancement occurs since the crystal does not absorb as strongly and the "out resonances" are even further away.

Fig. 16

Dose dependence study of Cd^{++} implanted cuprous oxide from ref. 2. The ion doses are: a) unimplanted; b) 1.5×10^{11} ions/cm; c) 1.5×10^{13} ions/cm; d) 1.5×10^{14} ions/cm . 476.5 nm excitation is used throughout and the base line for each spectrum has been translated.

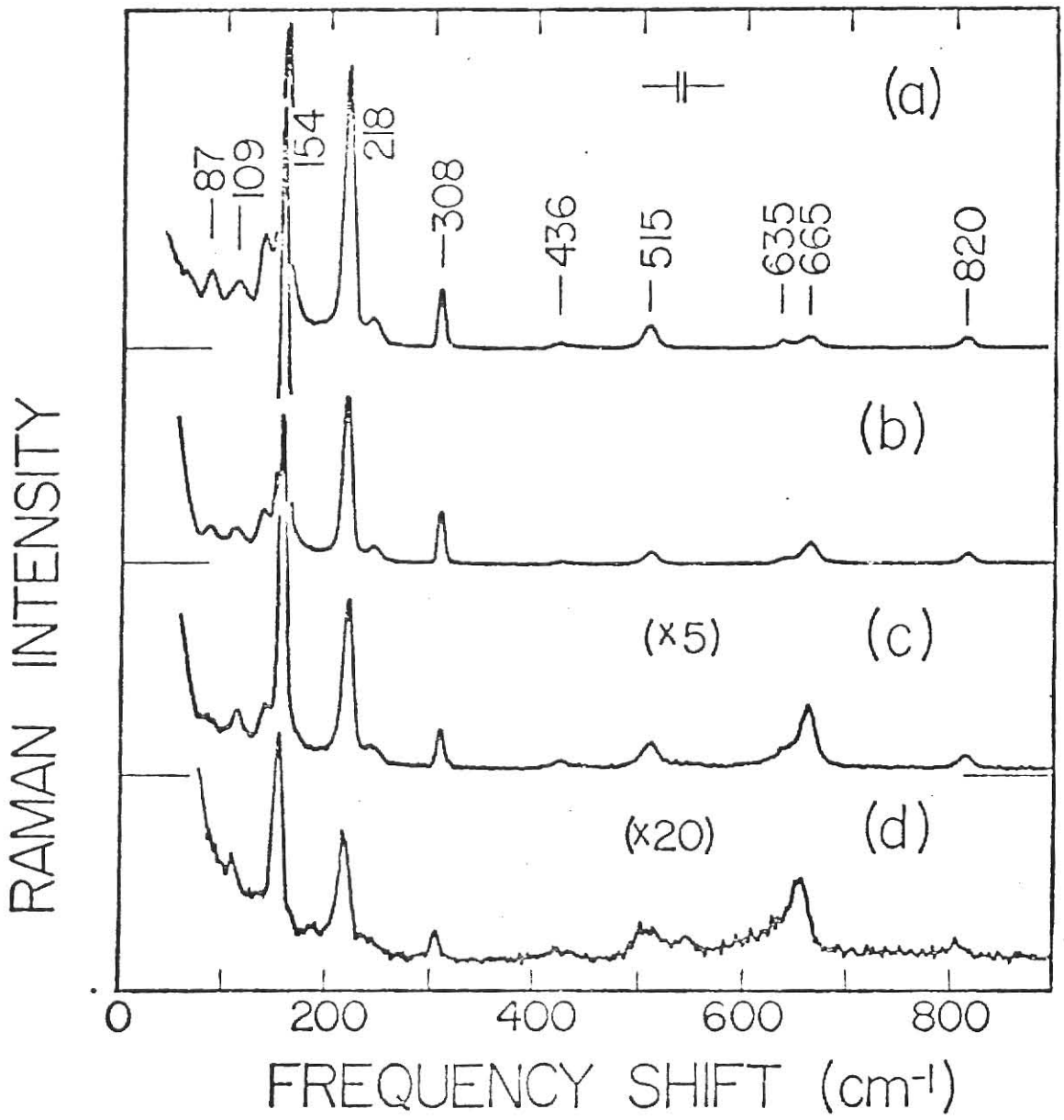
RAMAN INTENSITY
(a)
(b)
(c)
(d)
(x5)
(x20)
87
109
154
218
308
436
515
635
665
820
0
200
400
600
800
FREQUENCY SHIFT (cm⁻¹)

Fig. 17

Absorption spectrum for pure cuprous oxide from ref. 31. Superimposed are the positions of the argon ion laser frequencies used for the Raman scattering experiments. The peak absorption at 20,850 cm^{-1} corresponds to the 1s blue exciton of cuprous oxide.

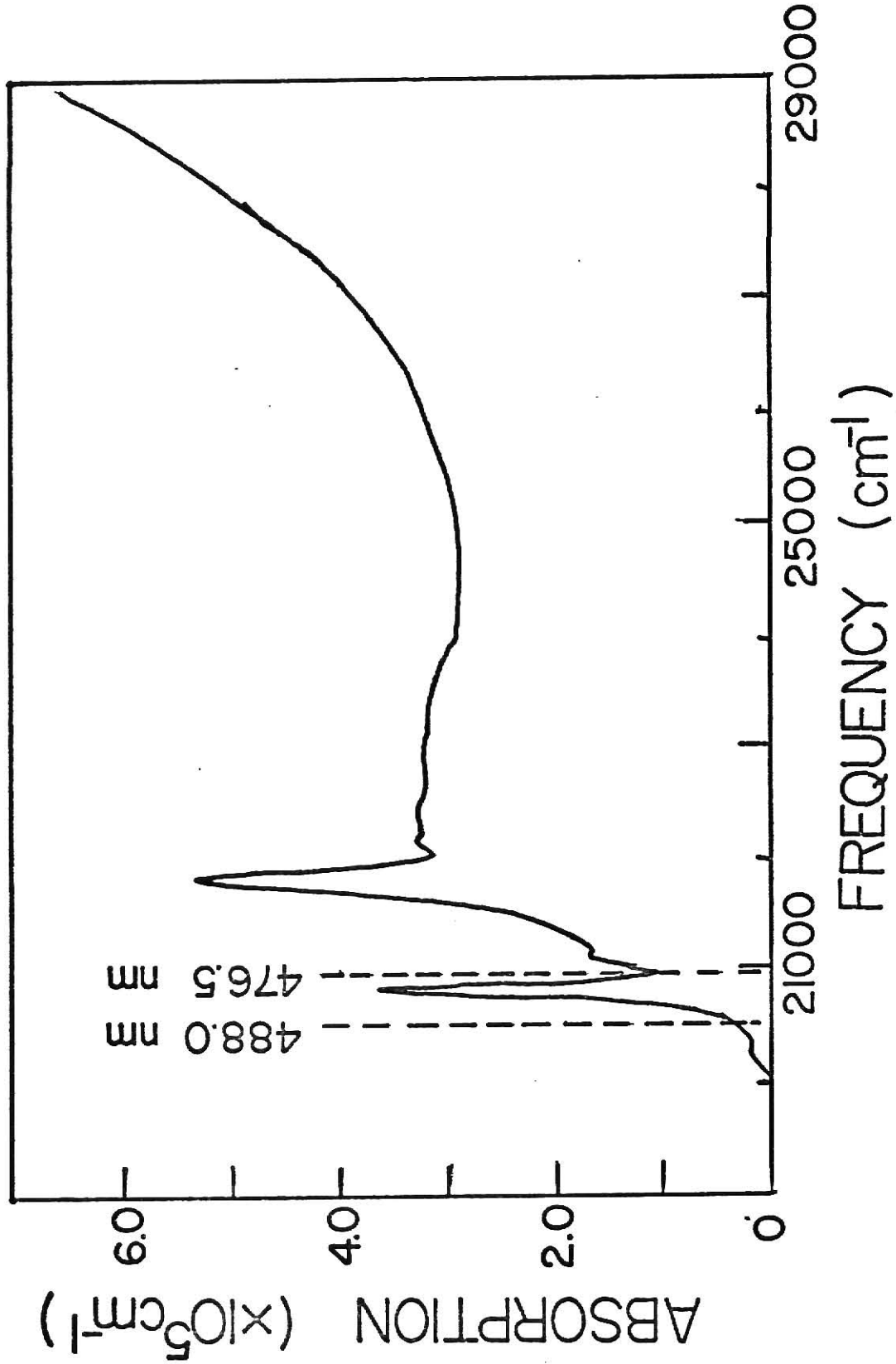
ABSORPTION (x10^{5}cm^{-1})
6.0
4.0
2.0
0
488.0 nm
476.5 nm
21000
25000
29000
FREQUENCY (cm^{-1})

Another important reason for choosing these two laser frequencies is their penetration depth into Cu_2O. From the absorption curve of Fig. 17, the penetration depths are estimated to be 0.1 μm for 476.5 nm and 0.3 μm for 488.0 nm excitation into a pure crystal. These depths are greater than the projected range of the Cd^{++} implants but are of the same order as the projected ranges of the Na^{+} and He^{+} implants. In the ideal case, one wants to match the penetration depth of the laser to the projected ranges of the ions so as to probe only the damaged layers of the crystal.

A test of the absorption has been done by Powell, et al.[2] in order to check the depth matching. In their work, they found that the intensity of the 154 cm^{-1} Raman feature for a 90 keV Cd^{++} implanted sample was ~2 times higher than that for a 180 keV Cd^{++} implant at the same ion dose with 476.5 nm excitation, but was nearly 50 times less intense than that for a pure, unimplanted sample. We know that the Raman intensity $I \propto V$, where V is the scattering volume. If the penetration depth of the laser into the damaged crystal matches the damage depth of the 180 keV implant, then the scattering volume is composed entirely of damaged crystal. For the 90 keV implant, the damage layer thickness is approximately one half of that for the 180 keV implant and so the scattering volume V is now composed of approximately one half damaged (and one half undamaged crystal). We assume that the absorption constant, α, does not change with damage. Then if for an undamaged crystal $I_{RAMAN} = I_0$, one expects that $I_{RAMAN} = \frac{1}{2}I_0$ for the case of the 90 keV implant where our scattering volume contains only one half undamaged crystal. The experimental results of ref. 2

show that $I_R = 1/50$ rather than $\frac{1}{2}I_0$. This means that the absorption must have increased greatly, enough that the penetration depth of the laser probably matches that, or at least, is not any greater than the damage depth of the implanted ions. So based upon experimental data, the laser frequencies used allow us to probe mostly damaged layers and little undamaged crystal.

If we assume the absorption due to excitons has a Gaussian line shape, then Fig. 18 shows how the absorption would behave as the exciton state broadens with damage. Assuming the number of absorbing centers (i.e. number of exciton states) remains constant, a decrease in the peak absorption at the exciton frequency is accompanied by an increase in the absorption in the wings.

The effects of this broadening on the Raman spectra can be seen by the superposition of a laser line (476.5 nm) and some of its corresponding Raman features (when we consider the 1s blue exciton). The 154 cm^{-1} feature is in an "out resonance" with the exciton. As the state broadens, the peak absorption decreases thus decreasing the strength of the coupling for the 154 cm^{-1} feature. The absorption increases for the laser line as expected but then decreases after a certain level of damage is reached. The 218 cm^{-1} feature behaves in a similar fashion though the amount of broadening is different at the point where the growth of the absorption changes sign. With 488.0 nm excitation, the absorption will probably increase rather uniformly for the laser line and its corresponding Raman features up to a certain level and then decrease uniformly with annealing.

Fig. 18

Behavior of a normalized Gaussian function as its full width is varied. This is probably how the absorption behaves in a damaged crystal as it is annealed. Trace a: little or no damage; trace d: probable damage saturation. Superimposed are some of the Raman features for 476.5 nm excitation illustrating how the various resonances behave with changing absorption.

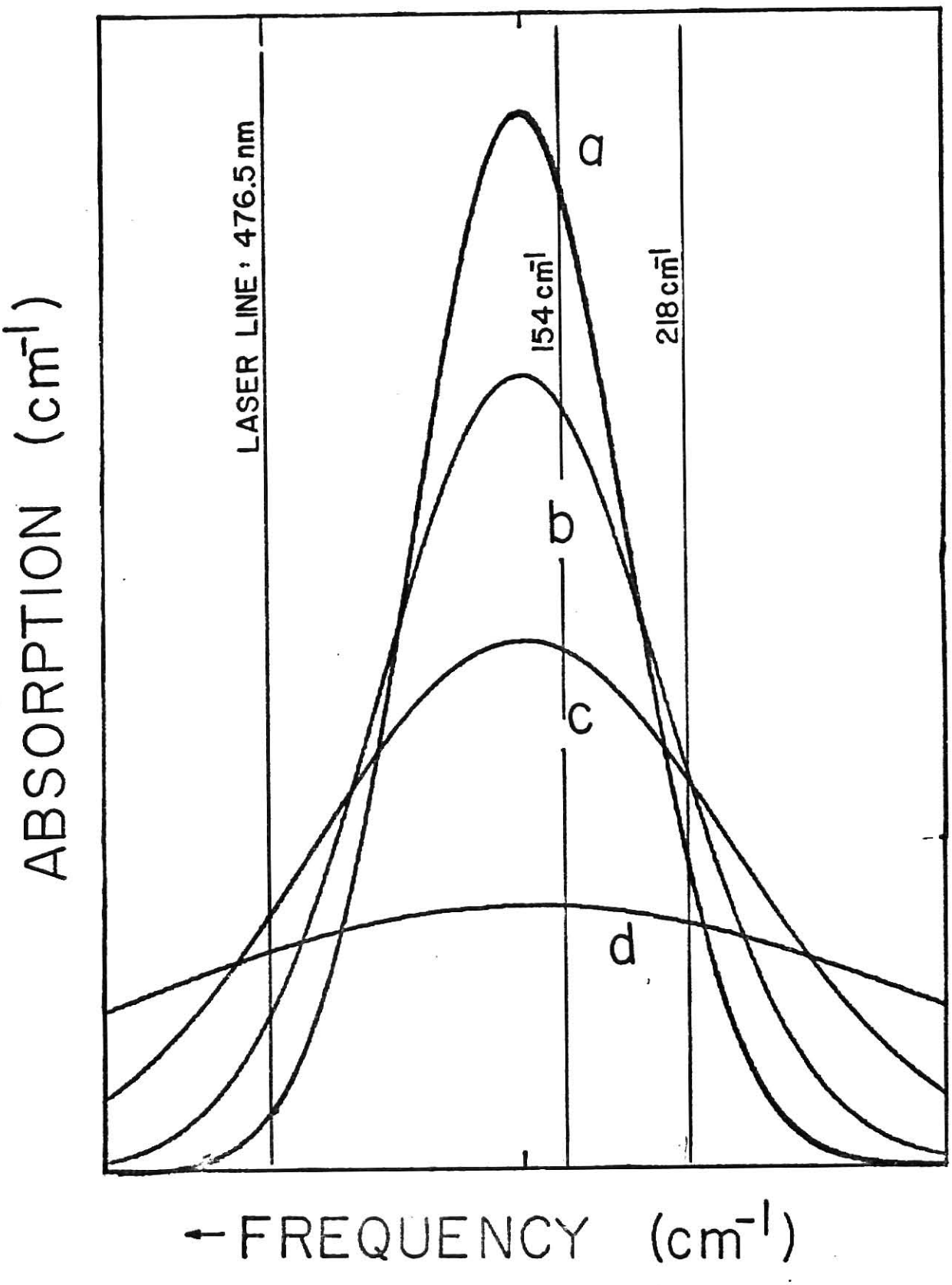
ABSORPTION (cm⁻¹)
LASER LINE : 476.5 nm
154 cm⁻¹
218 cm⁻¹
a
b
c
d
FREQUENCY (cm⁻¹)

Experimental Raman Data

A composite of Raman spectra of the Cd^{++} implant using 476.5 nm excitation is shown in Fig. 19. One observes generally large increases in the Raman intensities between the implanted, unannealed sample (trace a) and the pure, unimplanted sample edge (trace e). In particular, we focus our attention onto the 154 cm^{-1} and 218 cm^{-1} Raman features because these two modes are affected more by the resonance conditions than any other modes in Cu_2O, with the excitation frequencies used. We see the Raman intensity increases by factors of ~16 and ~50 for the 154 cm^{-1} and 218 cm^{-1} modes respectively. The rest of the traces in Fig. 19 illustrate the growth in intensity after each anneal treatment until the spectrum strongly resembles the spectrum of the unimplanted sample after the final anneal.

Plots of the peak heights versus anneal temperature, of the 154 cm^{-1} and the 218 cm^{-1} Raman features using 476.5 nm excitation, are shown in Figs. 20 -- 22 for the Cd^{++} implant, the Na^{+} implant and the He^{+} implant respectively. These peak heights were obtained, in each case, by subtracting out the background due to elastically scattered light in the Raman spectrum and then normalizing the intensities to a common excitation power for each series since $I_R \propto$ power of the laser. In each case, the samples were annealed until their pre-implantation Raman intensities were nearly restored.

Several similarities among Figs. 20 -- 22 are noted: i) large increases of one to two orders of magnitude occur as the annealing progresses; ii) an important annealing stage occurs in the temperature range of 270 - 310°C for the one-half hour anneal (Fig. 20) and in the range of 230 - 270°C for the one hour anneals (Figs. 21 and 22).

Fig. 19

Resonance Raman spectra for the Cd^{++} implanted cuprous oxide ("h") illustrating the annealing behavior for a series of 30 minute isochronal anneal treatments: a) 25°C; b) 230°C; c) 270°C; d) 310°C; e) unimplanted edge. Excitation is 476.5 nm.

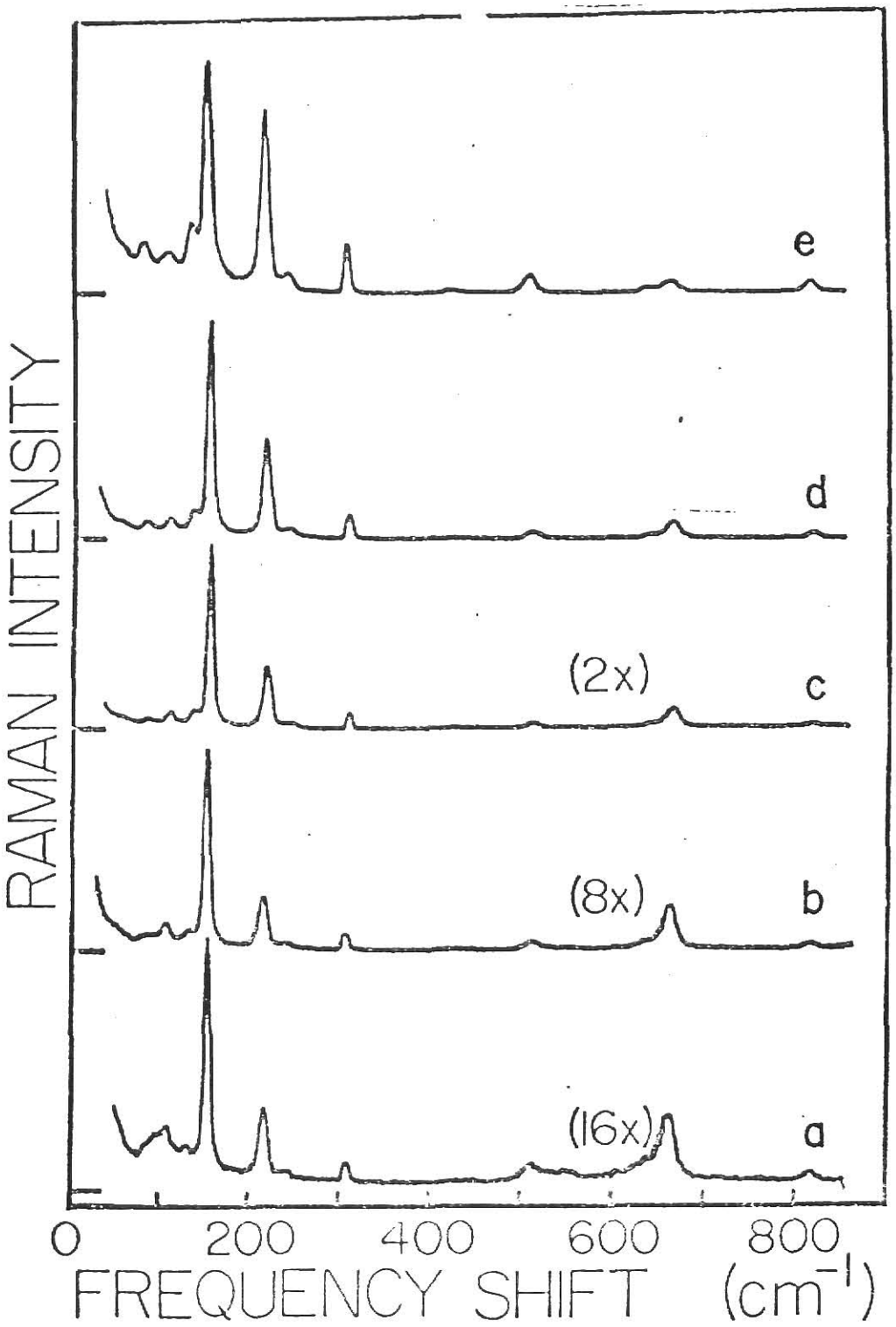
RAMAN INTENSITY
e
d
(2x)
c
(8x)
b
(16x)
a
0
200
400
600
800
FREQUENCY SHIFT (cm⁻¹)

Fig. 20

Plot of the Raman peak height as a function of anneal temperature for the Cd^{++} implanted cuprous oxide ("h"). This is for a series of 30 minute isochronal anneal treatments.

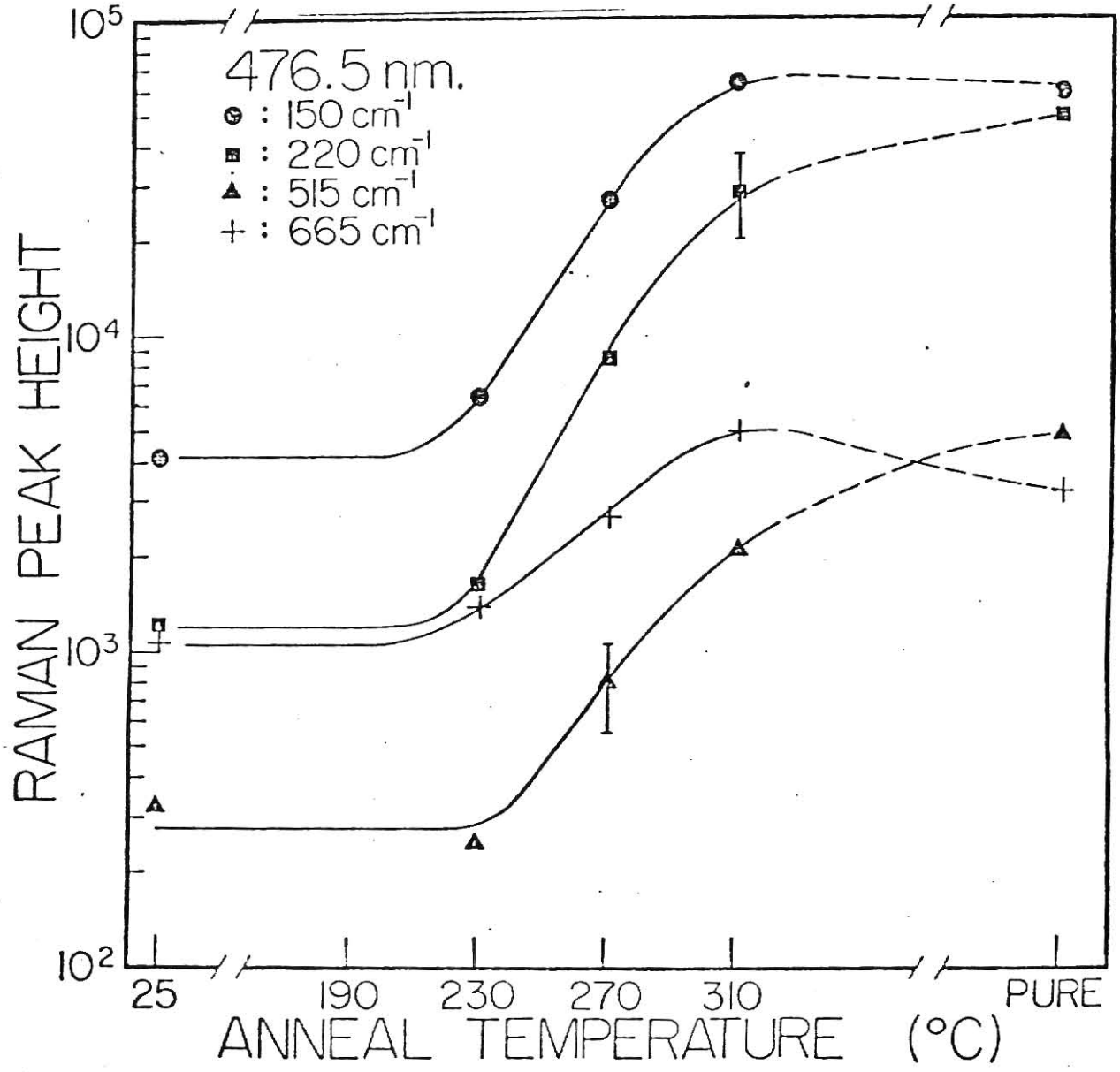
476.5 nm.
: 150 cm⁻¹
: 220 cm⁻¹
: 515 cm⁻¹
+ : 665 cm⁻¹
RAMAN PEAK HEIGHT
10⁵
10⁴
10³
10²
25
190
230
270
310
PURE
ANNEAL TEMPERATURE (°C)

Fig. 21

Plot of the Raman peak height as a function of anneal temperature for the Na^+ implanted cuprous oxide ("4"). This is for a series of 60 minute isochronal anneal treatments.

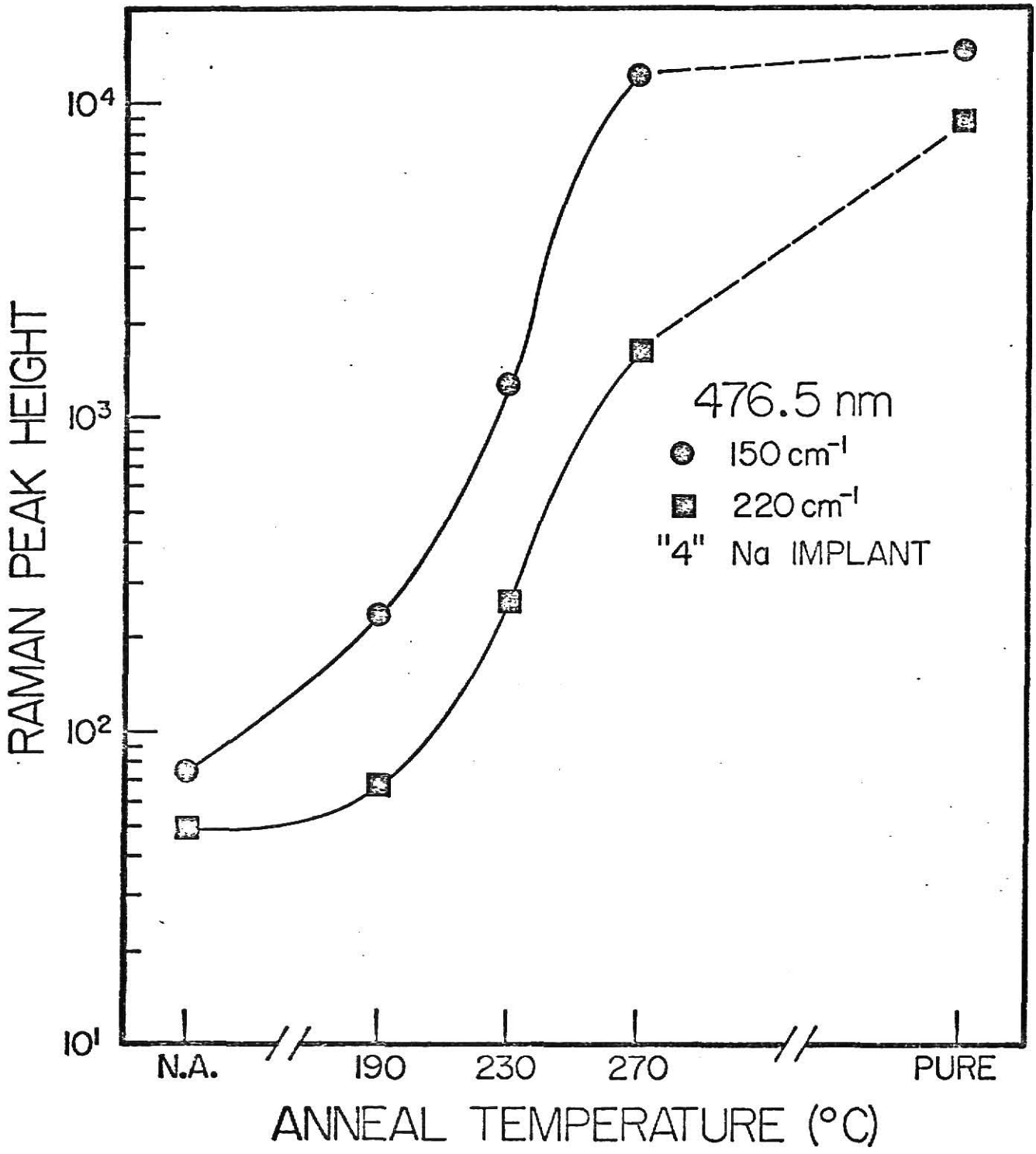
RAMAN PEAK HEIGHT
10^4
10^3
10^2
10^1
476.5 nm
150 cm^{-1}
220 cm^{-1}
"4" Na IMPLANT
N.A.
190
230
270
PURE
ANNEAL TEMPERATURE (°C)

Fig. 22

Plot of the Raman peak height as a function of anneal temperature for the He^+ implanted cuprous oxide ("9"). This is for a series of 60 minute isochronal anneal treatments.

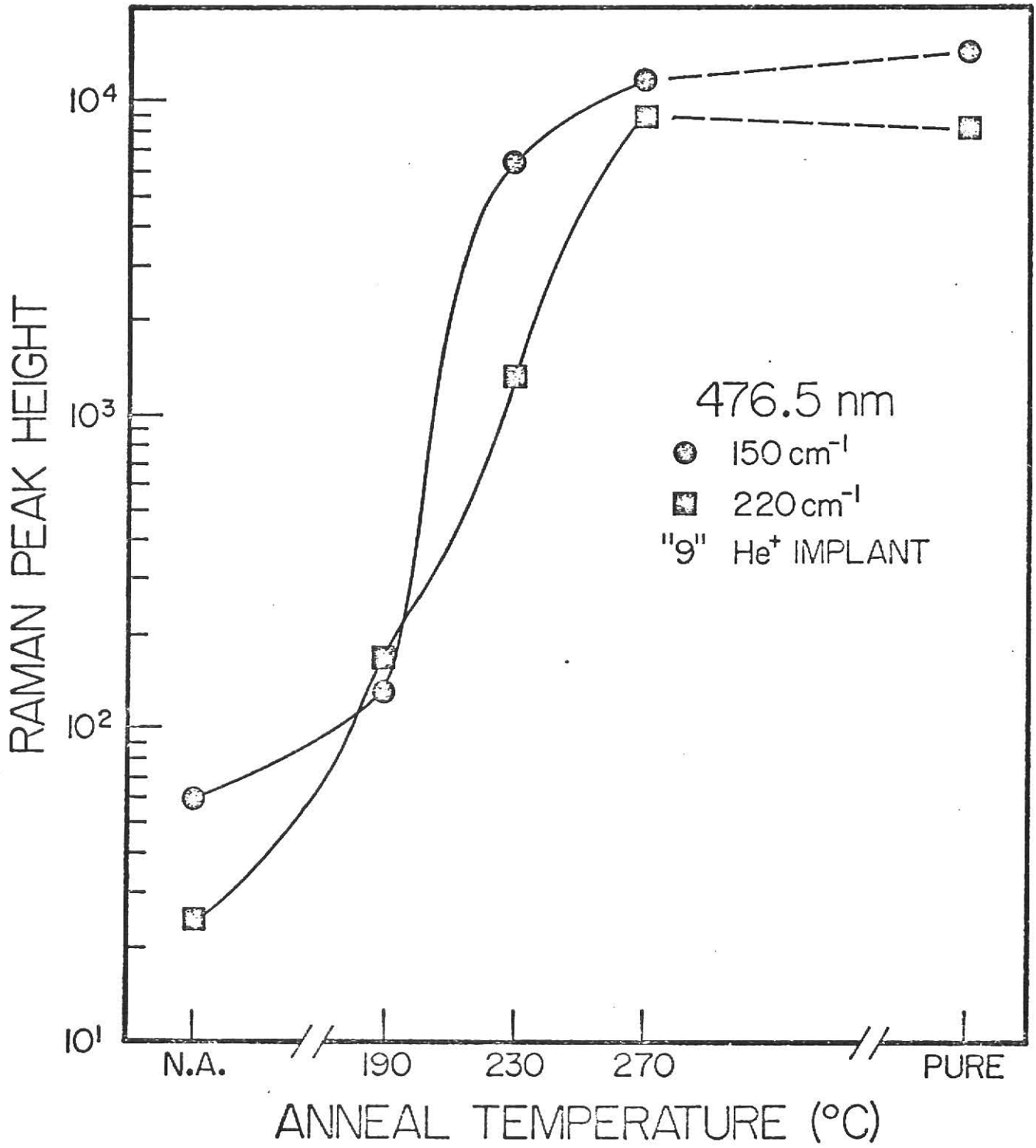
RAMAN PEAK HEIGHT
10^4
10^3
10^2
10^1
476.5 nm
150 cm^{-1}
220 cm^{-1}
"9" He$^+$ IMPLANT
N.A.
190
230
270
PURE
ANNEAL TEMPERATURE (°C)

Some differences also occur: i) a steeper rise in the peak height occurs for the lighter ion (He^{+}) than for the Na^{+} in the one-hour anneals (this suggests some annealing dependence upon either the type of ion specie implanted or the damage it creates); ii) after the final anneal treatment, little further improvement in Raman intensities probably would occur with continued annealing since the initial intensities are almost completely restored. The 218 cm^{-1} feature for the Na implant, however, is down some in intensity from where it probably would be if we had continued annealing this sample using temperatures higher than those used for the other implants.

Though it would appear that nearly all the damage has annealed out of the Cd^{++} implant, Fig. 23 shows some important departures. In Fig. 23 we have a composite of Raman spectra using 488.0 nm excitation on the same Cd^{++} implanted sample we studied with 476.5 nm excitation. 488.0 nm excitation is further away from resonance so its corresponding Raman spectrum does not have the resonance enhancement that the 476.5 nm spectrum has. However, two interesting observations are made here: i) In following traces a through e of Fig. 23, the 154 cm^{-1} feature seems to have reached a stage beyond which it neither grows further or decays. However, the 218 cm^{-1} feature would probably continue to grow while the 154 cm^{-1} feature would have to decrease in intensity in order to match the pre-implantation spectrum; ii) A second difference is in the intensities of the 635 cm^{-1} feature and the 665 cm^{-1} features. For the unimplanted sample, $I(635\ cm^{-1}) > I(665\ cm^{-1})$, where as for the implanted, annealed sample (trace d), $I(635\ cm^{-1}) < I(665\ cm^{-1})$.

Fig. 23

Raman spectra for the Cd implanted cuprous oxide ("h") illustrating the annealing behavior for a series of 30 minute isochronal anneal treatments: a) 25°C; b) 230°C; c) 270°C; d) 310°C; e) unimplanted edge. Excitation here is 488.0 nm.

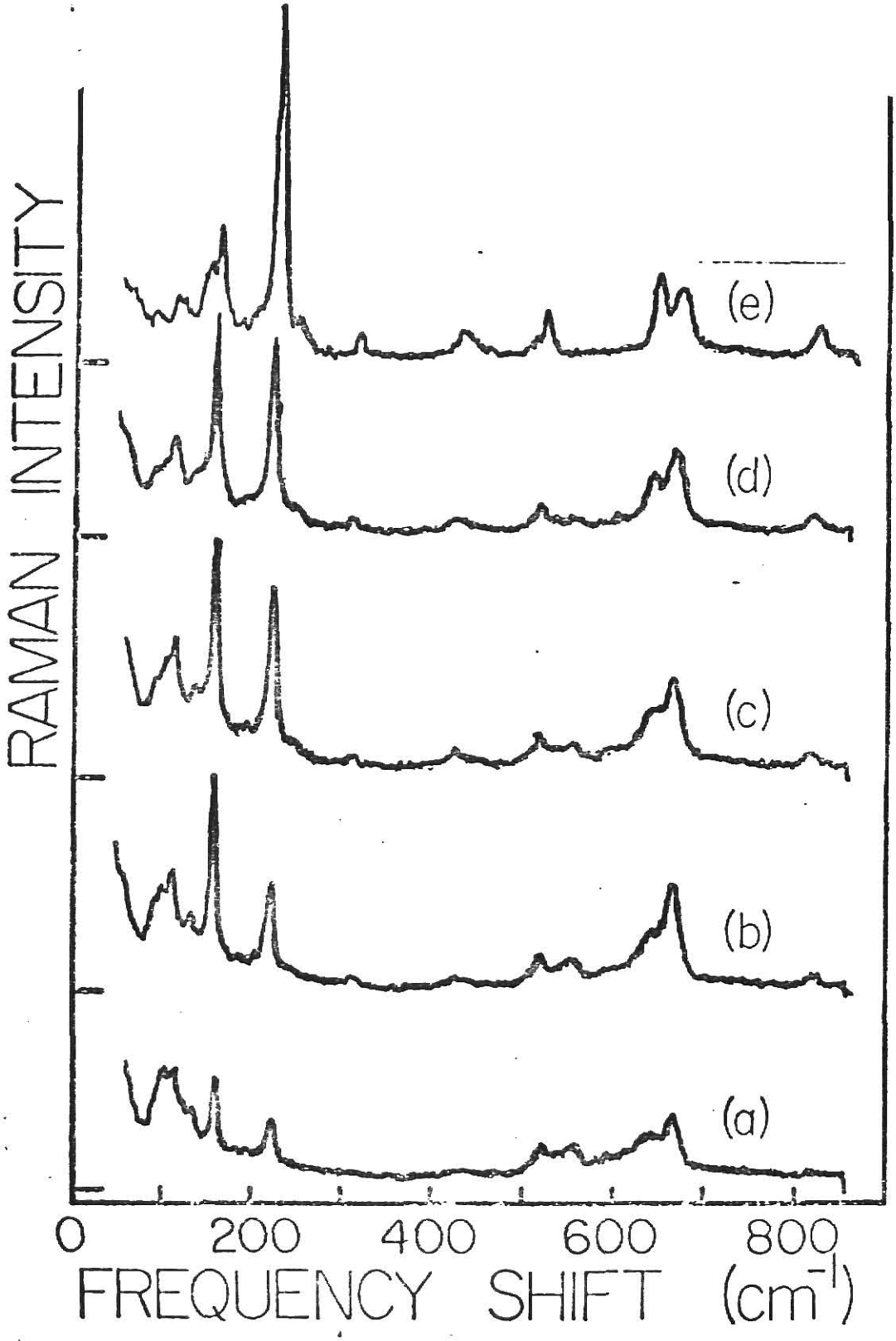
RAMAN INTENSITY
(e)
(d)
(c)
(b)
(a)
0
200
400
600
800
FREQUENCY SHIFT (cm⁻¹)

Fig. 24

Plot of the Raman peak height as a function of anneal time for the Cd implanted cuprous oxide ("d") illustrating the annealing behavior for a series of isothermal anneal treatments at 230°C. Excitation is 476.5 nm.

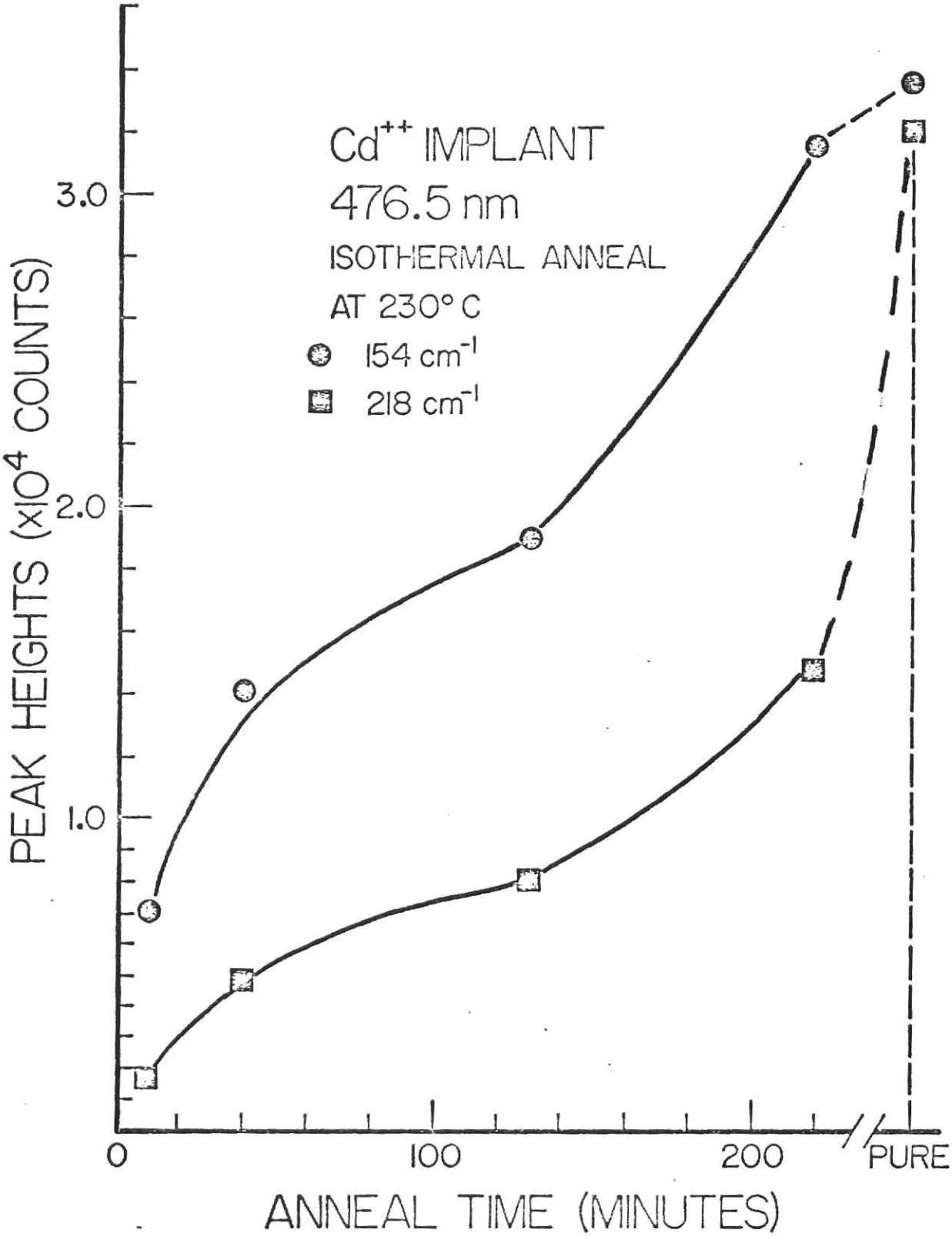
Cd++ IMPLANT
476.5 nm
ISOTHERMAL ANNEAL
AT 230° C
154 cm-1
218 cm-1
PEAK HEIGHTS (x10^4 COUNTS)
3.0
2.0
1.0
0
100
200
PURE
ANNEAL TIME (MINUTES)

Fig. 24 shows the results of a series of isothermal anneal treatments on another Cd^{++} implanted sample with 476.5 nm excitation. While showing the usual growth of the Raman features, after a final anneal of four hours at 230°C, complete recovery of Raman intensities has not occurred. The 218 cm^{-1} feature is down in intensity by over a factor of 2. However, comparison to Fig. 19 for the isochronal anneal treatments of a Cd^{++} implant also show the 218 cm^{-1} feature to be down in intensity by nearly a factor of 2 after its final anneal at 310°C - 1/2 hour. The significant point here is that it will probably take an anneal treatment of many hours in length to anneal almost all the damage out at a temperature of 230°C, where as it took only one hour to anneal most all the damage at a temperature of 310°C. 230°C could probably be considered as a lower limit on the damage annealing temperature. Since it takes in excess of four hours to anneal effectively at 230°C, the jump frequency, f, is probably not very large.

Discussion of Results

The growth of the Raman intensities corresponds to increases in the undamaged portion of the scattering volume. However, this is complicated by the resonance conditions at hand. We must consider both the coupling of the incident photon to the exciton states and the scattered photon to the exciton states. The nature of this coupling is discussed in Ref. 2. The strength of this coupling depends upon the broadening of the exciton absorption bands as we saw in discussion of Fig. 18. For 476.5 nm excitation, the large increases in intensity of the 154 cm^{-1} Raman feature with increasing anneal temperature are due to increasing resonance as the 1s blue exciton state narrows.

We have seen that the Raman intensities increase to nearly their pre-implantation level as the lattice damage anneals. This is because as the lattice periodicity is restored, so are the scattering selection rules. This is strongly supported by the appearance of a weak feature at 550 cm^{-1} in the Raman spectrum for all the implanted samples prior to any anneal treatments. This feature initially did not show up in the pure crystal spectra; it gradually annealed away and was completely gone by the final anneal. It is probable that this feature resulted from a phonon whose frequency is 550 cm^{-1} at the Brillouin zone boundary, as shown in Fig. 4, and it appeared because the selection rules restricting the photon scattering to the center of the zone were relaxed. It is doubtful that the feature was due to localized modes from the placement of the ions since it usually requires some annealing to activate and locate implanted ions and because it occured in the same place regardless of the type of ion implanted. Localized modes would vary with the atomic mass and could conceivably even vary from one sample to the next with the same implanted ion, depending upon the dose and annealing parameters.

Damage in Cu_2O appears to anneal significantly at 250°C. This is a low temperature when compared to post growth anneal temperatures of approximately 1000-1050°C.[27]

The differences in Figs. 19-21 which we pointed out earlier are probably due to the type of ion implanted. An interpolation of the nuclear stopping curves of Fig. 1 shows that 92 keV Na into Cu_2O has an Sn = 380 $keV/_{micron}$ which is nearly 50 x greater than that for 60 keV He into

Cu_2O. Since the He dose is 20 x larger than the Na dose, we expect the damage density near the surface to be 2-3 x higher for the Na implant. The differences between the annealing of the He implant and the Na implant may be due to the difference in the damage density. Of course it is possible the differences may be due to the atomic sizes of the ions since Na is larger and may create more complex type of damage. A similar argument concerning the Cd ions was already presented when we discussed the reflectivity data.

From Fig. 4 of Ref. 2, we see that the Raman intensities decrease by a factor of 100 when the ion dose increases from 10^{11} to 10^{14} ions/$_{cm^2}$. Since our Cd ions were in doses of 10^{14} ions/$_{cm^2}$ and since we observed increases of a factor of 100 in intensity with annealing, the damage level corresponding to 10^{14} ions/$_{cm^2}$ probably annealed to a level corresponding to 10^{11} ions/$_{cm^2}$. This change suggests that probably no more than 0.1% of the initial damage remains after the final anneal.

Though 0.1% seems to be a tiny amount of damage left, Fig. 23 shows us that significant perturbations remain. After the final anneal, use of 488.0 nm excitation shows that the 154 cm^{-1} feature is more intense than its 218 cm^{-1} neighbor and is also more intense than it is in the unimplanted spectrum. Significant coupling to the 1s and 2s exciton states which are still broadened exists. This occurs because the narrowing of the exciton states was accompanied initially by increasing absorption in this region 500-600 cm^{-1} from the 1s state. After some level of annealing is reached, the absorption then starts to decrease as inferred from the Gaussian peak

of Fig. 18. We have apparently reached this turning point in our annealing. Additional annealing is expected to result in a reduction in the intensity of the 154 cm^{-1} feature for 488.0 nm excitation since we would be weakening the coupling resonance.

C. Extrinsic Luminescence

While the purpose of ion implantation is to introduce ions which may enhance the electrical and optical properties of a semiconductor, this is not an easy objective to achieve in practice. We have seen no direct evidence indicating that the Cd and He have become optically active during the anneal treatments. However, the Na implant showed some unusual luminescence in the implanted region where none had previously occurred after a series of one hour isochronal anneals to 270 C. Figure 25 shows a composite of Raman spectra, using various Argon laser excitation frequencies from 20,986 cm^{-1} (476.5 nm) to 21,834 cm^{-1} (457.9 nm), arranged on the absolute frequency scale to determine any excitation frequency dependence. No consistent frequency shift of the peak position from the incident excitation frequency is evident. While the Raman features show their appropriate and expected shifts (with excitation frequency), the broad feature remains essentially stationary. This shows that we do have luminescence. A check of an unimplanted edge of the same sample revealed no broad features, thus the luminescence is not due to undamaged crystal annealing effects. It is probable that the luminescence is due to the activation of the Na since none of the other implanted samples showed any activation at all. We have superimposed the position of the 1s blue exciton feature (80 K) showing its close proximity to our luminescence feature. The nearness of the two features suggests that an important interaction may be occuring. The luminescence is shifted to lower energies relative to the exciton energy. Shifts to Lower energy in Ag doped Cu_2O have been observed

Fig. 25

Raman spectra of the Na implanted cuprous oxide ("4") plotted on the absolute frequency scale. Note the position of the broad luminescence feature as the excitation frequency is changed.

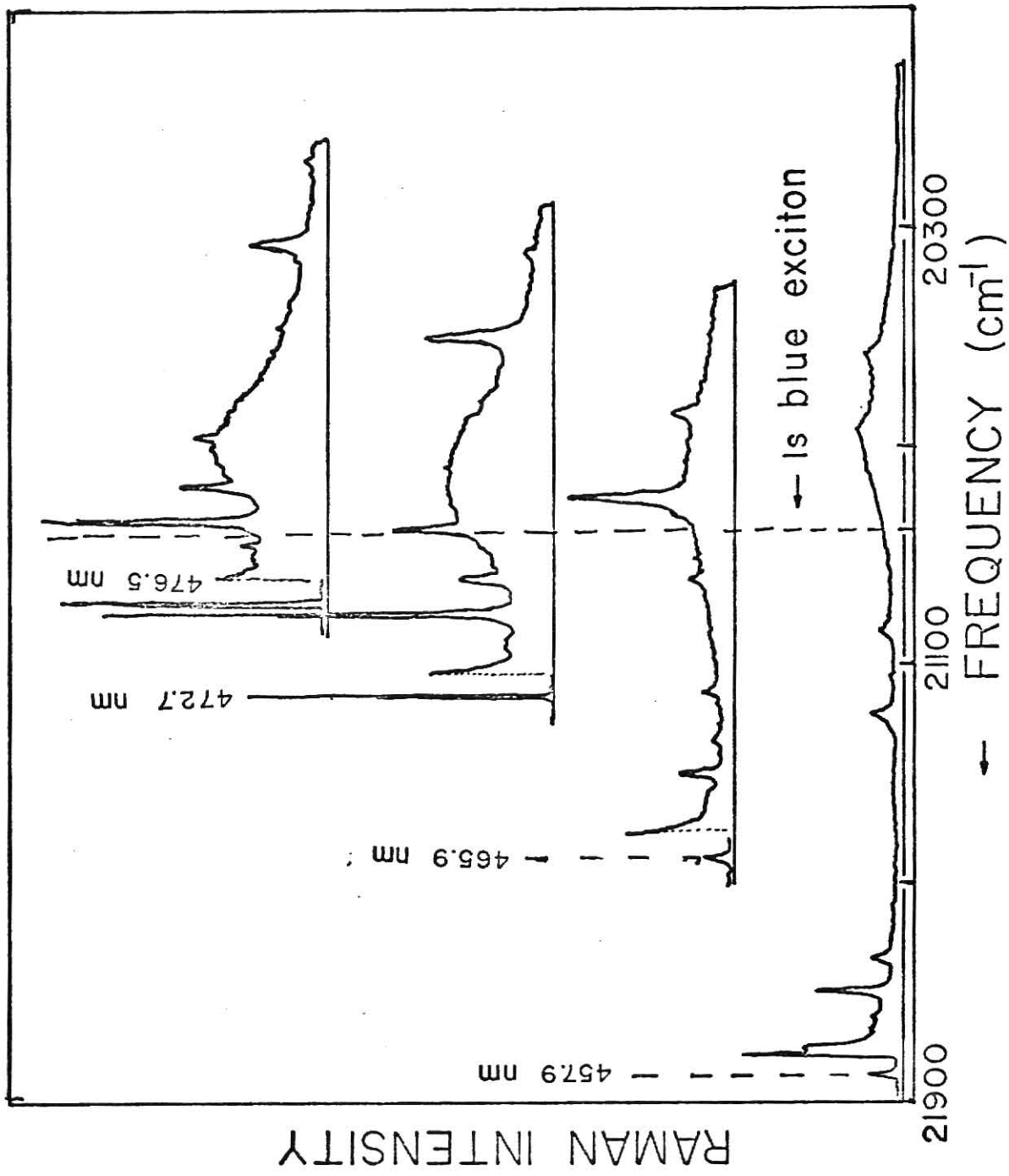
RAMAN INTENSITY
457.9 nm
465.9 nm
472.7 nm
476.5 nm
1s blue exciton
21900
21100
20300
FREQUENCY (cm⁻¹)

in the yellow exciton region,[35] so that our shift is entirely reasonable.

Figure 26 shows a plot of the peak position's dependence upon laser excitation for sample temperatures of 20 K and 80 K. Generally, the peak shifts to lower energies as the temperature decreases. The position of the 1S blue exciton at 80 K is plotted for reference. At 20 K, the 1s blue exciton shifts by 100 cm^{-1} to higher energies.[36] However, we find that our luminescence peak shifts in the opposite direction relative to the shift of the 1S blue exciton as the temperature decreases.

If we consider the bound exciton complex discussed earlier, the binding energy is the difference between the exciton energy and the energy of the peak luminescence. Taking the 1s blue exciton state at 20,850 cm^{-1}, the binding energy is found to vary between 23.58 meV (190 cm^{-1}) and 9.93 meV (80 cm^{-1}) at a sample temperature of 80 K. According to the earlier discussion, the bound exciton spectrum is supposedly composed of a series of discrete, sharp spectral lines, however, since the exciton states are 100 cm^{-1} broad (from the reflectivity data), a broad luminescence peak for bound excitons might also be expected.

Before proceeding further, we should examine another possible explanation for the luminescence: that of the free-bound transition discussed earlier. Here the width of the luminescence is attributed to the thermal energy, kT, of the free particle. This means that if we change the sample temperature from 80 K to 20 K, the width ought to decrease by a factor of 4. When the sample was cooled to 20 K, the width did decrease but only about 10% and certainly not by a factor of 4. This tells us

Fig. 20

Plot of the peak position of the luminescence as a function of excitation frequency for two different temperatures. The position of the 1s blue exciton at 20 K is off scale and in the direction of increasing frequency relative to its position at 80 K.

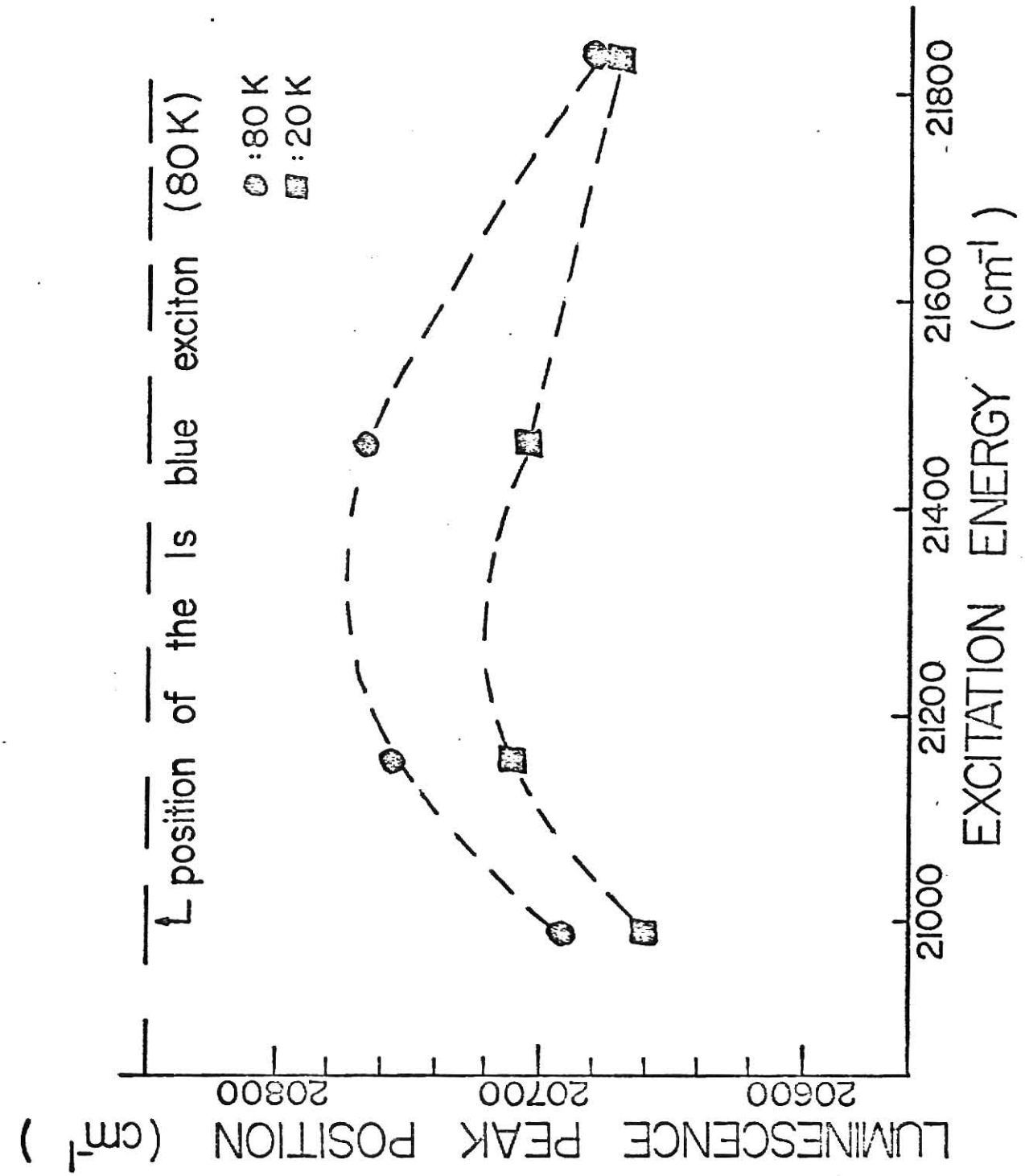
LUMINESCENCE PEAK POSITION (cm⁻¹)
20600
20700
20800
EXCITATION ENERGY (cm⁻¹)
21000
21200
21400
21600
21800
position of the ls blue exciton (80K)
: 80 K
: 20 K

that this latter model proposed probably would not explain the luminescence very well.

The relative shifting of the luminescence with exciton frequency at a single temperature is not clear. This shifting occurs at both temperatures, though it is not as great at 20 K as it is at 80 K. A shift to lower energies for lower temperatures has been observed in the photoluminescence due to impurities in n type GaAs in the infrared (λ>829.0 nm).[37] One possible cause of the shifting may be due to possible resonance conditions between the luminescing mechanisms and the applied excitation and/or even the Raman features.

V. Summary and Conclusions

Resonance Raman scattering has been shown to be a sensitive probe of ion-implantation-produced damage and its subsequent annealing in Cu_2O. The use of laser frequencies nearly resonant with intrinsic exciton states allow us to probe the lattice damage to a depth nearly equal to the thickness of the damage layer in addition to producing intense Raman features whose changes in intensity with damage make this technique especially sensitive to lattice damage. The ability to control the projected range of the implanted ions to match the absorption depth of a pure crystal makes this technique highly versatile for damage studies. Increases in the Raman intensities of up to a factor of 100 occur with the gradual annealing of the damage. It is found that a strong anneal stage occurs at 250°C which is significant when compared to typical post growth anneal temperatures of up to 1050°C. Comparisons with a dose

dependence study done in this laboratory suggests that probably less than 0.1% of the initial damage remains after our final anneal treatment.

Optical reflectivity experiments performed in conjunction with the Raman studies indicate that the blue and violet exciton states broaden considerably with damage to the extent that excitons probably do not exist in Cu_2O that has been made amorphous by ion implantation. It is desirous to do a Kramers-Kronig analysis of the reflectivity data in order to see just how the absorption and the index of refraction behave as the damage anneals out and the lattice periodicity is restored. Of interest is how this behavior compares to the broadening of a Gaussian or a Lorentzian line shape peak. The reflectivity data can be improved with a more careful pre-implantation sample polishing in addition to using higher quality samples.

Optical activity has been obtained in the Na^+ implanted sample. Luminescence occurs which is probably due to a bound exciton-impurity complex with a binding energy between 10 and 23 meV, depending upon the excitation frequency. This suggests additional experiments to investigate the behavior of this luminescence. A high resolution scan of the luminescence band may yield information as to its composition, that is, whether it is an envelope of a series of sharp, closely spaced spectral peaks or if it is actually a single broad band. A detailed study of the unusual behavior of the extrinsic luminescence peak position with excitation frequency may also yield some significant results concerning bound exciton-impurity complexes.

References

1. A. Compaan; Solid State Comm. 16 293 (1975).
2. D. Powell, A. Compaan, J. R. MacDonald, R. A. Forman; Physical Review B 12 20 (1975).
3. Bruce J. Pierce; Thesis "Luminescence and Hall Effect of Ion Implanted Layers in ZnO"; Air Force Institute of Technology. Wright-Patterson AFB, Ohio, Sept. 1974.
4. C. E. Barnes, C. B. Norris, H. J. Stein, W. Beezhold; in Ion Implantation in Semiconductors and Other Materials ed. B. Crowder; Plenum Press, 1973. p. 333.
5. D. D. Sell & A. U. MacRae; Journal of Applied Physics 41 4929 (1970).
6. S. H. Wemple, J. C. North, J. M. Dishman; Journal of Applied Physics 45 1578 (April 1974).
7. K. H. Eklund and Å. Anderson, in Ion Implantation in Semiconductors and other Materials, ed. B. Crowder; Plenum Press, 1973. p. 275.
8. Y. Kato et al. in Radiation Damage and Defects in Solids, by The Institute of Physics, London, 1972. p. 348.
9. A. H. Kachare, W. G. Spitzer, F. K. Euler, A. Kahan; Journal of Applied Physics 45 2938 (1974).
10. A. H. Kachare, W. G. Spitzer, A. Kahan, F. K. Euler, T. A. Whatley; Journal of Applied Physics 44 4393 (1973).
11. A. H. Kachare, J. M. Cherlow, T. T. Yang, W. G. Spitzer, F. K. Euler; Journal of Applied Physics 47 161 (1976).
12. J. E. Davey, T. Pankey, P. R. Malmberg, W. H. Lucke; Applied Physics Letters 17 323 (1970).

13. G. A. Shifrin & R. G. Hunsperger; Applied Physics Letters 17 274 (1970).

14. P. S. Peercy; Applied Physics Letters 18 574 (1971).

15. Further references on ion implantation and damage production are:

a) James F. Gibbons; Proc. IEEE 60 1062 (1972).

b) James F. Gibbons; Proc. IEEE 56 295 (March 1968).

c) Mayer, Eriksson, Davies; "Ion Implantation in Semiconductors" Academic Press; New York, 1970.

d) Wilson, Brewer; "Ion Beams; With Applications to Ion Implantation", John Wiley & Sons, New York 1973.

16. William S. Johnson, James F. Gibbons "Projected Range Statistics in Semiconductors" 1970. (Both authors are of Stanford University). The computations in this book are based upon the model of energy loss and range developed by:

J. Lindhart, M. Scharff, and H. E. Schiott; K. Dan. Vidensk. Selsk. Mat. Fys. Medd. 33, 14 (1963). This model is popularly called the "LSS." The book of Johnson and Gibbons contains a computer program one may use to calculate the stopping powers for various energies in addition to computing the projected range of the ions, which will be used later on. In addition to the computer program, Johnson and Gibbons have computed stopping powers and ranges for numerous types of ions into a number of semiconductors and have such data tabulated in the book. This data will become useful later on in making projected range estimates for ion species into Cu_2O which were not included in the calculations by D. D. Dragsdorf.

17. M. M. Beg & S. M. Shapiro; Physical Review B 13, 1728 (1976).

18. G. W. Chantry; The Raman Effect Vol. 1 (Ed. A. Anderson) M. Dekker Inc., New York, 1971.

19. R. Cowley; The Raman Effect Vol. 1 (Ed. A. Anderson) M. Dekkar Inc., New York, 1971.

20. A. Pinczuk, E. Burstein; Topics in Applied Physics: Vol. 8 "Light Scattering in Solids" (Ed. M. Cardona) Springer-Verlag Publ. New York, 1975.

21. P. F. Williams; Thesis (Ph.d) Dept. Electrical Engineering, University of Southern California, Feb. 1973.

22. B. I. Boltaks; Diffusion in Semiconductors translated by J. I. Carasso. Academic Press, New York (1963).
See, for example Chapter 4.

23. R. C. Fletcher & W. L. Brown; Physical Review 92 585 (1953).

24. James F. Gibbons; Proc. IEEE 60, 1062 (1972), (See pp. 1087-1089).

25. J. P. Dahl & A. C. Switendick; J. Phys. Chem. Solids; 27, 931 (1966).

26. Dean; "Electroluminescence" in Applied Solid State Science Vol. 1 (1969) Ed: R. Wolfe, p. 9, 59.

27. W. S. Brower, Jr., H. S. Parker; J. Crystal Growth 8, 227, (1971).

28. A. J. Dekkar; "Secondary Electron Emission" in Solid State Physics: Advances in Research and Applications Vol. 6 (1958); Ed: F. Seitz; D. Turnbull, Academic Press, New York, 1958; p. 254-257.

29. J. B. Grun, M. Sieskind, S. Nikitine; J. Phys. Chem. Solids; 19, 189 (1961).

30. C. E. Hathaway & L. A. Rahn; Rev. Scientific Instruments: 43, 294 (February 1972).

31. P. F. Williams, S. P. Porto; Phys. Rev. B 8, 1782 (August 1973).

32. R. Knox; "Theory of Excitons" Supplement #5 to Solid State Science, H. Ehrenreich; F. Seitz; D. Turnbull; eds. Academic Press, New York, 1963.

33. R. J. Elliot in "Polarons and Excitons", Ed: C. G. Kuper and G. D. Whitfield; Scottish Universities Summer School, 1962, Oliver and Boyd, London, 1963.

34. Richard Bube; The Electronic Properties of Crystalline Solids Academic Press. New York, 1974.

35. M. Grosmann in "Polarons and Excitons", Ed. C. G. Kuper, G. D. Whitfield, Scottish Universities Summer School, 1962; Oliver and Boyd, London, 1963.

36. The assumption is made that the blue exciton series shifts in the same direction in energy as do the yellow and green exciton series when the temperature is changed. An interpolation from the yellow and green excitons to the blue exciton is made using the data of Ref. 29.

37. Takeshi Kamiya and Elmar Wagner; J. Appl. Phys.; 47, 3219 (July, 1976).

38. C. Carabatos, B. Prevot; Phys. State Sol. (b) 44, 701 (1971).

RESONANCE RAMAN SCATTERING AND OPTICAL REFLECTIVITY STUDIES OF ION IMPLANTATION-PRODUCED DAMAGE IN CUPROUS OXIDE

by

JOSEPH FREDRICK HESSE

B. S., University of Nebraska, 1974

AN ABSTRACT OF A MASTER'S THESIS

submitted in partial fulfillment of the

requirements for the degree

MASTER OF SCIENCE

Department of Physics

KANSAS STATE UNIVERSITY
Manhattan, Kansas

1977

Abstract

We have used Raman scattering to study ion implantation-produced damage and its annealing characteristics in Cu_2O. Chemically etched crystals were implanted at room temperature with 60 keV He^+, 92 KeV Na^+, and 184 KeV Cd^{++} ions in doses ranging from 1.6×10^{13} to 10^{16} ions/cm^2. These samples were then annealed with series of 30 or 60 minute isochronal anneals up to 410°C in Argon gas. We have found that Raman spectra, obtained with laser frequencies nearly resonant with intrinsic exciton states, are very sensitive to the damaged layer, ~300 Å deep, and the lattice damage subsequently anneals at ~250°C. After annealing to 270°C, the Na^+ implant develops a blue luminescence centered at ~20,690 cm^{-1} with a full width at half maximum of ~200 cm^{-1} at 100 K, just below the 1s blue exciton.